

Evaluating the Impact of the COSMIC RO Bending Angle Data on Predicting the Heavy Precipitation Episode on 16 June 2008 during SoWMEX-IOP8

SHU-CHIH YANG

Department of Atmospheric Sciences, National Central University, ZhongLi, Taiwan

SHU-HUA CHEN

University of California, Davis, Davis, California

SHU-YA CHEN

University Corporation for Atmospheric Research, Boulder, Colorado

CHING-YUANG HUANG AND CHING-SEN CHEN

Department of Atmospheric Sciences, National Central University, ZhongLi, Taiwan

(Manuscript received 22 August 2013, in final form 2 July 2014)

ABSTRACT

Global positioning system (GPS) radio occultation (RO) data have been broadly used in global and regional numerical weather predictions. Assimilation with the bending angle often performs better than refractivity, which is inverted from the bending angle under spherical assumption and is sometimes associated with negative biases at the lower troposphere; however, the bending angle operator also requires a higher model top as used in global models. This study furnishes the feasibility of bending-angle assimilation in the prediction of heavy precipitation systems with a regional model. The local RO operators for simulating bending angle and refractivity are implemented in the Weather Research and Forecasting (WRF)–local ensemble transform Kalman filter (LETKF) framework. The impacts of assimilating RO data from the Constellation Observing System for Meteorology Ionosphere and Climate (COSMIC) using both operators are evaluated on the prediction of a heavy precipitation episode during Southwest Monsoon Experiment intensive observing period 8 (SoWMEX-IOP8) in 2008. Results show that both the refractivity and bending angle provide a favorable condition for generating this heavy rainfall event. In comparison with the refractivity data, the advantage of assimilating the bending angle is identified in the midtroposphere for deepening of the moist layer that leads to a rainfall forecast closer to the observations.

1. Introduction

Heavy rainfall frequently appears in Taiwan during the early summer rainy seasons (mid-May to mid-June; [Chen and Chen 2003](#)), especially over southwestern Taiwan ([Chen et al. 2007](#)). To investigate the mechanism of the heavy rainfall in this region of complex terrain ([Fig. 1a](#)), the Southwest Monsoon Experiment (SoWMEX) and the Terrain-Influenced Monsoon Rainfall Experiment

(TiMREX) were conducted jointly during the period from 15 May to 30 June 2008 in the northern South China Sea (SCS), and the western coastal plain and mountain slope regions of southern Taiwan ([Jou et al. 2011](#)). The objectives of SoWMEX/TiMREX are to improve understanding of physical processes associated with terrain-influenced heavy precipitation systems and the monsoon environment in which they are embedded, and ultimately, to better forecast heavy rain-producing convective systems. The issuing of flash flood warnings has become a challenging task in Taiwan due to the complex terrain and limited observations associated with the dynamic and thermodynamic fields. The availability of the global positioning system (GPS) radio occultation (RO) observations

Corresponding author address: Shu-Chih Yang, Department of Atmospheric Sciences, National Central University, 300 Zhong-Da Rd., ZhongLi 32001, Taiwan.
E-mail: shuchih.yang@atm.ncu.edu.tw

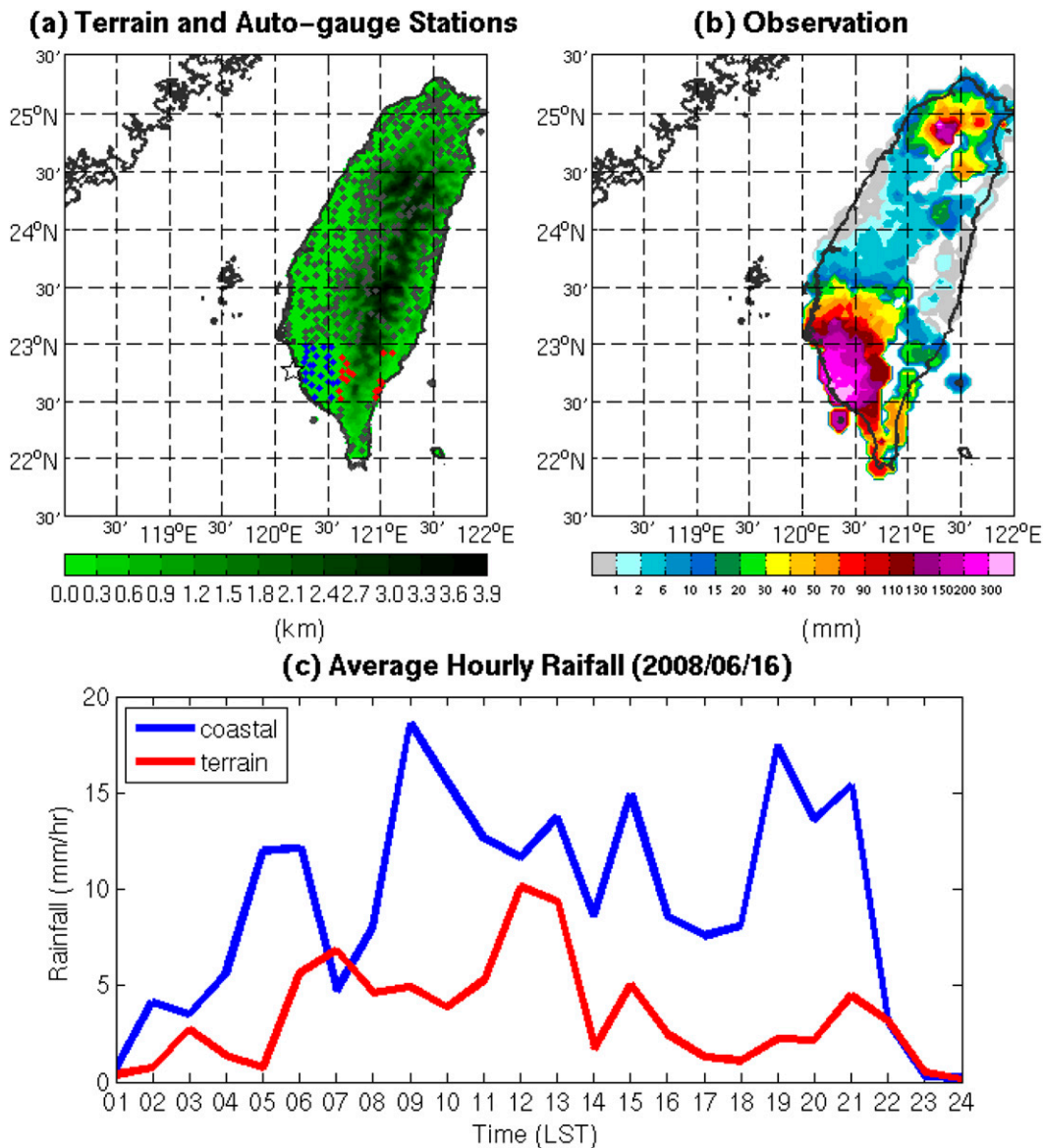


FIG. 1. (a) Topography of Taiwan (km) and the distribution of the automatic rain gauge stations. The blue and red diamonds are used to indicate the rain gauges in the coastal and terrain regions, respectively. (b) Total accumulated rainfall on 16 Jun from the observations in color scale (mm). The star in (a) denotes the model grid point (22.8°N, 120.2°E) near the Tainan sounding station. (c) Time series of the hourly rainfall from the automatic rain gauges. The coastal and terrain rainfall are computed based on the rain gauges, denoted by blue and red dots, respectively, in (a).

provides the possibility to depict the temperature and moisture profiles of the atmosphere (Kursinski et al. 1997; Kuo et al. 2000).

During recent years, GPSRO observations have been well recognized as improving global analysis and prediction with operational numerical weather prediction (NWP) systems (Healy and Thépaut 2006; Cucurull et al. 2006, 2007; Healy et al. 2007; Cucurull and Derber 2008; Aparicio et al. 2009; Anlauf et al. 2011). Benefits are attributed to high accuracy and precision with high vertical

resolution (2–60 m up to the stratosphere), all-weather capability little shadowed by cloud, and equal accuracy over both land and ocean (Anthes et al. 2008). Mainly, improvements are identified in the temperature fields since the moisture concentrates in the low troposphere where the amount of the RO data is limited. Baker (2011) demonstrates that the Constellation Observing System for Meteorology Ionosphere and Climate (COSMIC) RO data provides highly useful observation impact and effectively reduces the 1-day forecast error. Aiming to

assimilate the upstream GPSRO data, Healy et al. (2007) and Healy (2008) use the European Centre for Medium-Range Weather Forecasts (ECMWF) operational global four-dimensional variational data assimilation (4D-Var) system to show that the GPSRO bending angle data have a positive impact on temperature analysis and forecast in the mid- to upper troposphere and stratosphere. Cucurull et al. (2013) suggest that assimilation of the RO bending angle can be more beneficial than RO refractivity data in terms of the NWP forecast skill, with the challenge of vertical water vapor gradients and larger residual errors from the ionospheric correction. However, among these works, the impact of GPSRO data on low-troposphere moisture is less clear.

For regional weather prediction, studies have shown that assimilating the RO-retrieved refractivity data is beneficial for predicting the typhoon track and heavy precipitation (Huang et al. 2005, 2010; Chen et al. 2009; Kueh et al. 2009). Recently, a case study by Liu et al. (2012) showed that when RO refractivity was assimilated using a quasi-excess phase operator, moisture in the boundary and wind analysis at the low and upper troposphere were enhanced, leading to more accurate genesis and intensification of Hurricane Ernesto (2008). In addition to the impact on tropical cyclones, the impact of assimilating RO refractivity data to improve the simulated mei-yu frontal systems is discussed in Huang et al. (2010). However, negative impacts are found in the moisture field at the 850-hPa level. As a consequence, the expected ability of the RO data to improve the moisture convergence and thus the heavy rainfall may be limited.

In most of the current data assimilation systems, assimilation of the retrieved local RO refractivity data is commonly performed for simplicity since one only needs to interpolate modeled pressure, water vapor, and temperature values from the model grid points to the observation locations (Cucurull et al. 2007). However, the local refractivity operator with a spherically symmetric assumption can correctly simulate the refractivity only when the atmosphere/model is locally spherically symmetric. It has been shown that RO refractivity contains negative bias (thus dry bias) in the lower troposphere with super-refraction mostly stemming from the Abel inversion under spherical symmetry assumption (Sokolovskiy 2003; Cucurull et al. 2013; Vergados et al. 2013). Also, inaccuracies may be introduced by using the climatology or auxiliary information to retrieve refractivities from bending angle profiles (Kuo et al. 2000). Because there is no use of an Abel inversion, bending angle is regarded as the upstream data and it is also expected that the measurement error is less correlated in the bending angle than in refractivity profiles. Therefore, it is preferable to assimilate

the bending angle observation. Studies show that most of the global atmospheric assimilating systems use the local operator to assimilate the RO bending angle and that the advantage of using the upstream bending angle data can still be valid as compared with the refractivity data (Healy and Thépaut 2006; Cucurull et al. 2013). In this study, a local operator for deriving the local bending angle from model local refractivity is used to investigate the impact of assimilating the bending angle. The observation operator is further described in section 3b.

Nonlocal operators for refractivity (i.e., excess phase) and bending angle have been proposed in earlier studies (Sokolovskiy et al. 2005b) to take into account the horizontal gradient of the atmosphere by integrating the refractivity along a ray. Studies (Sokolovskiy et al. 2005a,b; Chen et al. 2009; Ma et al. 2009, 2011) prove that using the nonlocal operator for the excess phase provides better analysis than using the local refractivity operator. However, in addition to concern regarding the computational efficiency, the nonlocal operator for assimilating the excess phase could have the same limitations since it also still uses refractivity. Healy et al. (2007) found that both local and two-dimensional nonlocal bending angle operators obtain similar results in the global model forecast, given the consideration that the limited accuracy of observations is characterized in the lower troposphere because of the processing methods. It is meaningful to demonstrate the feasibility of local bending angle assimilation in the regional model.

The impact of RO data for mesoscale weather prediction has been investigated in previous studies; however, these mostly use the local operator for assimilating refractivity. With the experience of the global assimilation system, the upstream RO bending angle data are expected to better represent local variations. In this study, the RO products of refractivity and bending angle are assimilated with local operators in the Weather Research and Forecasting–local ensemble transform Kalman filter (WRF–LETKF) system (Yang et al. 2012). The error covariance in the WRF–LETKF system can represent the local flow-dependent dynamical uncertainties and naturally carries local properties of terrain. This helps better spread out the observation corrections for updating the model state during the assimilation. The goal of our study is to examine the feasibility of assimilating COSMIC RO moisture information for predicting a localized heavy precipitation event, through a case study in June 2008 during SoWMEX/TiMREX.

This paper is organized as follows: section 2 introduces the synoptic conditions that produced an extreme heavy rainfall event in Taiwan. The data assimilation system used in this study is discussed in section 3. Section 4

describes the design of data assimilation and numerical experiments, while section 5 presents the analyses and forecasts in terms of factors leading to heavy precipitation. Section 6 discusses the results from a series of sensitivity experiments related to the assimilation of bending angle data. Finally, the conclusions are given in section 7.

2. A brief overview of the characteristics of heavy rainfall on 16 June 2008 during the SoWMEX/TiMREX IOP8 event

The IOP8 event during SoWMEX/TiMREX (Tu et al. 2014; Davis and Lee 2012; Xu et al. 2012) is characterized by active convective cells in the coastal region of southwestern Taiwan, resulting in heavy precipitation on 16 June in this region (Fig. 1b). As shown in the observations [Figs. 17, 18 of Xu et al. (2012)], the convection embedded in the southwesterly wind initialized offshore southwestern Taiwan and moved inland.

At 0000 UTC 16 June, a mesoscale cyclone was present over southern China at the 850-hPa level [Fig. 4d of Xu et al. (2012)] and a strong southwesterly flow (or low-level jet, LLJ) with warm moist advection was observed over the northeastern SCS and southwestern Taiwan coast [Figs. 6, 7 of Xu et al. (2012)]. The southwesterly LLJ over the upstream ocean of southwestern Taiwan that conveys abundant moisture was deflected to a southerly flow by Taiwan's topography [Fig. 8 of Xu et al. (2012)], resulting in a low-level convergence over the coast of the southwestern Taiwan. Such a local convergence produces favorable conditions for the development of heavy precipitation systems. Because of the persistent rainfall over southwestern Taiwan and the adjacent coast from 14 to 15 June, a cold pool with a temperature depression of 2°–4°C in the lowest 500 m formed there (Davis and Lee 2012; Xu et al. 2012). Tu et al. (2014) also indicate that the cold pool over southwestern Taiwan and the adjacent ocean was further enhanced by the land breeze. As the convective systems propagated inland, intensification took place because of the warm, moist south-southwesterly flow interacting with the cool air associated with the land breeze. In addition, the low-level convergence between the deflected southerly flow due to orographic blocking (Fig. 1a) and the upstream southwesterly wind generated favorable conditions for the intensification of convection. Furthermore, the effect of orographic lifting aloft was absent due to the mountain-parallel flow. These important factors result in orographic blocking and the convective cells becoming active in the coastal region. Consequently, the heavy precipitation was

coastally orientated and limited over the terrain slope, as shown in Fig. 1b, based on the automatic rain gauge observations.

In this study, the assimilation period is from 0000 UTC 13 June to 1800 UTC 16 June. Whether heavy rainfall, in association with features discussed above, can be captured by analyses and forecasts is investigated in section 5. Particularly, we focus on the impact of the COSMIC-RO data in predicting the heavy precipitation on 16 June. As discussed in Davis and Lee (2012), important features for this event include that the heavy rainfall propagates from offshore to the coast, and the rainfall rate over the coastal region is always higher than the one over the terrain region (Fig. 1c). Before the overland precipitation starts, strong southerly wind appears offshore of southwestern Taiwan. The southerly wind is fundamental for localizing the rainfall over the coastal plain, given the humid environmental conditions. Compared to other heavy rainfall events during the SoWMEX/TiMREX field experiment (Lai et al. 2011), the rainfall intensity on 16 June is not only heavy but also long lasting (over 12 h), which leads to accumulated precipitation with a maximum more than 300 mm over coastal areas within 24 h. The difficulty in predicting this event is the location of the heaviest rainfall, which is crucial for issuing warnings of flood, landslide, or mudflow.

3. Data assimilation system and observation operators

a. The WRF-LETKF system

The data assimilation system used in this study is the LETKF (Hunt et al. 2007) coupled with the Advanced Research WRF Model, version 3.2 (Skamarock and Klemp 2008 and also <http://www.wrf-model.org/index.php>). The LETKF algorithm belongs to the square root filter and updates the ensemble mean and perturbations according to the local information of the background (a short-range forecast) and regional observations. This system has applied to study the issues in typhoon assimilation and prediction (Yang et al. 2012) and shows a reasonable skill with a real case of 2008 Typhoon Sinlaku (Yang et al. 2013). The details of the WRF-LETKF system are referred to Yang et al. (2012).

In addition to a 15% multiplicative covariance inflation (Anderson and Anderson 1999), covariance localization is used to avoid unrealistic correlation related to sampling issue and is important for optimizing the performance of LETKF. It is applied to the observation error covariance (Hunt et al. 2007) to increase the observation error with a Gaussian function in relating the distance between the

observation and analysis grid point. The e -folding localization scale used in this study is 350 km and the cutoff scale is 1000 km.

In the WRF–LETKF system, a gross error quality check (QC) procedure is applied to the observations before performing the analysis. If the difference between the observation and background state (i.e., innovation) is 5 times larger than the observation error, that particular observation is rejected. To better use the bending angle data in the low atmosphere, such QC for COSMIC data below 1 km is turned off. Further details about the experimental settings using the WRF–LETKF system are discussed in [section 4](#).

b. Local operators for the radio occultation

Local operators for simulating the RO refractivity and bending angle have been implemented into the WRF–LETKF system. The model local refractivity profile is calculated based on the model temperature, pressure and water vapor pressure [Eq. (A2)]. Here, “local” means using the model information at the occultation column, instead of the actual value following the ray by solving the ray-tracing equation, under the assumption of local symmetry.

The local bending angle operator has been developed at the National Central University (NCU), Taiwan ([Chen et al. 2010](#)). An Abel transform is applied to the local bending angle operator in order to inverse the model’s local refractivity profile to the local bending angle. Below the model top, the operator evaluates the bending angle integration according the vertical distribution of the refractivity, while above the model top, the bending angle is computed by extrapolating the uppermost model parameters as presented in [Healy and Thépaut \(2006\)](#). Detail of the local observation operator for RO bending angle is provided in the [appendix](#). Verification (the [appendix](#)) shows that the local bending angle derived by our observation operator gives reliable and comparable accuracy compared to the ECMWF Radio Occultation Processing Package (ROPP) operator based on [Healy and Thépaut \(2006\)](#).

We note that the assumption of exponential variation of the refractivity within each layer used in [Healy and Thépaut \(2006\)](#) is not applied to the NCU operator. Such an assumption may not be valid when strong vertical moisture gradient occurs, such as in the lower troposphere of warm and humid regions. [Figure 2a](#) shows an example of a moisture profile taken from a region having a high moisture content and sharp vertical moisture gradient in the low troposphere. In comparison, the variation of the vertical gradient of the temperature is relatively linear. Dominated by the moisture field the refractivity has a very strong vertical gradient

below 900 m [shown with $\ln(N)$ in [Fig. 2b](#)], resulting in a large bending angle greater than 0.05 rad between 300 and 500 m. Similar values are also obtained when using the ECMWF ROPP operator. With these unusual values, the observations will be rejected with the regular QC check. To demonstrate that such large values are due to the moisture gradient, not the accuracy of the operator, the moisture below 1 km is linearly interpolated between the first and seventh model levels, indicated by the red line in [Fig. 2a](#). After the modification of the moisture in the low levels, the logarithm of refractivity below 1 km behaves more linearly and the large values of the bending angle disappear (the dashed line in [Fig. 2b](#)). This also suggests how sensitive the bending angle is to the moisture, especially the larger vertical gradient near the boundary layer height. During the experiment period, the RO observations over the warm and moist region are near super-refraction and they play a crucial role in enhancing the moisture content (see [section 5a](#)). To preserve the impact of low-level RO bending angle observations in the assimilation experiments, the QC check below 1 km atmosphere was turned off. Note that when a severe situation of super-refraction occurs in observations, both bending angle and refractivity are both ill conditioned and are not used in assimilation.

Following [Healy and Thépaut \(2006\)](#), the observation error of the bending angle is assumed to be 10% at the surface and linearly decreases with height to 1% at 10 km. The observation error of the refractivity follows [Chen et al. \(2011\)](#), varying from 3% near the surface to 0.3% at 14 km. The primary focus of this study is to investigate the impact of the RO data on the prediction of the heavy precipitation system, in which the moisture plays a critical role. Given that most of the moisture resides in the lower troposphere and dominates the low-level RO signals, only the RO data below 5 km are assimilated in the experiments.

We note that assimilating only low-level RO data can avoid the model bias at higher levels. The WRF Model used in this study may have some cold bias near the model top and such cold bias can reach to 5 K after a two-day integration. However, such a cold bias has very limited influence on the simulation of the low-level bending angle. With even a cold bias as large as 15 K at the model top, it contributes less than 1% variation for the simulation of the bending angle below 5 km. Besides, the top of a regional model, which usually is much lower than that used in global models, may introduce nonnegligible errors and bias for simulating bending angle at higher altitude. The uncertainty associated with the use of a lower model top in the regional model is further discussed in [section 6b](#).

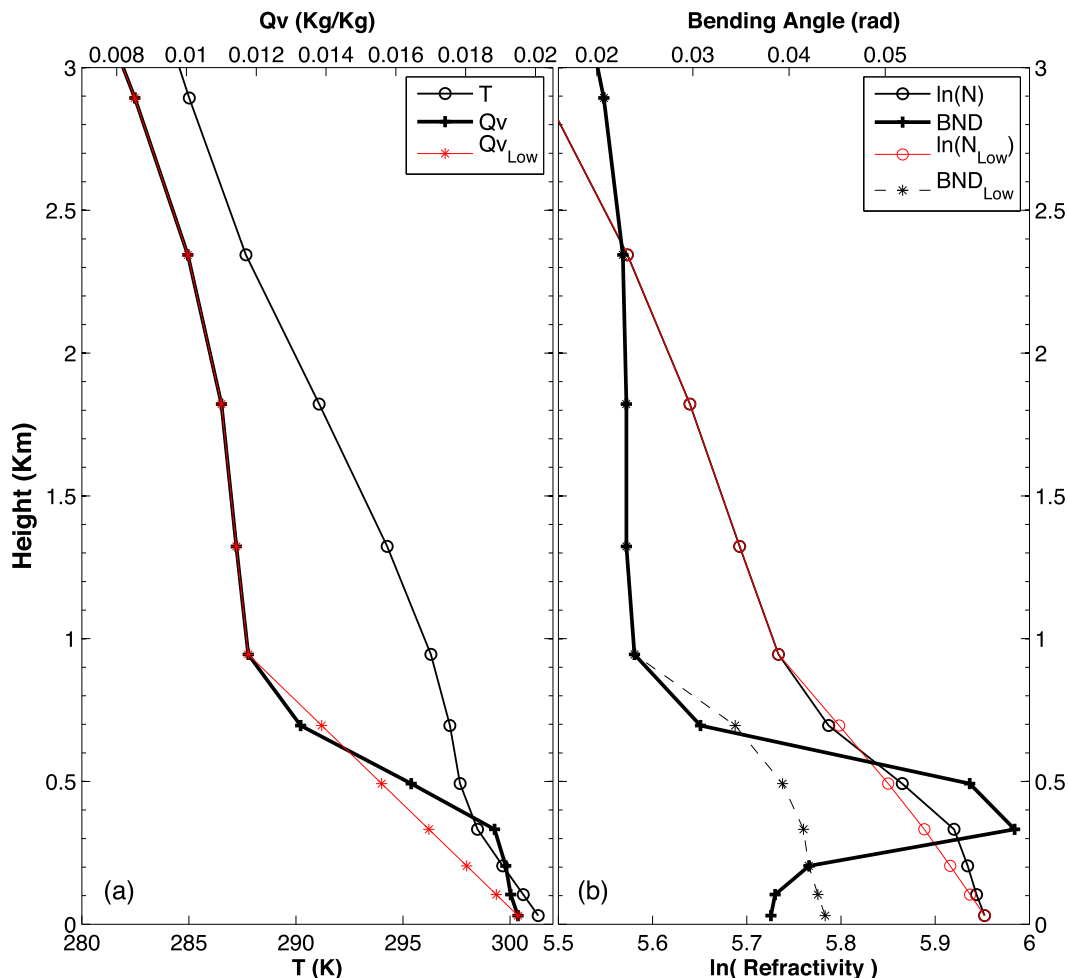


FIG. 2. (a) Model temperature (T , open circles) and water vapor mixing ratio (Q_v , asterisks) for a profile located in the region of the southwesterly jet. The red line denotes the new water vapor mixing profile, similar to the original one except that the values between the first and seventh model levels are modified. (b) Model refractivity (open circles) and bending angle (asterisks) profiles based on the information from (a). The modified refractivity and bending angle derived with the modified moisture are denoted as red and dashed lines, respectively.

4. Data assimilation and forecast experiment design

The WRF-LETKF system is used for all assimilation and numerical experiments in this study. Domain 1 (the largest domain in Fig. 3), the only domain that performs LETKF assimilation, uses a horizontal grid of 180×150 grid points with 27-km spacing. There are 27 vertically stretched layers, with the top at about 50 hPa. The physical parameterizations include the Rapid Radiative Transfer Model (RRTM) based on Mlawer et al. (1997) for longwave radiation, the Dudhia (1989) shortwave radiation scheme, the Yonsei University (YSU) PBL scheme (Hong et al. 2006), the Grell-Devenyi ensemble scheme (Grell and Dévényi 2002) for the cumulus parameterization, and the Goddard Cumulus Ensemble

(GCE) microphysics scheme (Tao et al. 2003). Starting at 1800 UTC 11 June 2008, a set of 36 ensemble forecasts are generated with initial conditions centered at the National Centers for Environmental Prediction (NCEP) Global Forecast System (GFS) Final Analysis (FNL $1^\circ \times 1^\circ$ data). The ensemble perturbations are randomly drawn based on the 3D-Var background error covariance (Barker et al. 2004). The same procedure is used to perturb the NCEP FNL data every 6 h until 0000 UTC 17 June; the tendencies are then computed at the boundaries according to these perturbed model states in order to obtain corresponding boundary conditions (Torn et al. 2006).

The WRF-LETKF analysis is performed every 6 h at 0000, 0600, 1200, and 1800 UTC, and the observations are collected with ± 3 -h windows. Observations used in

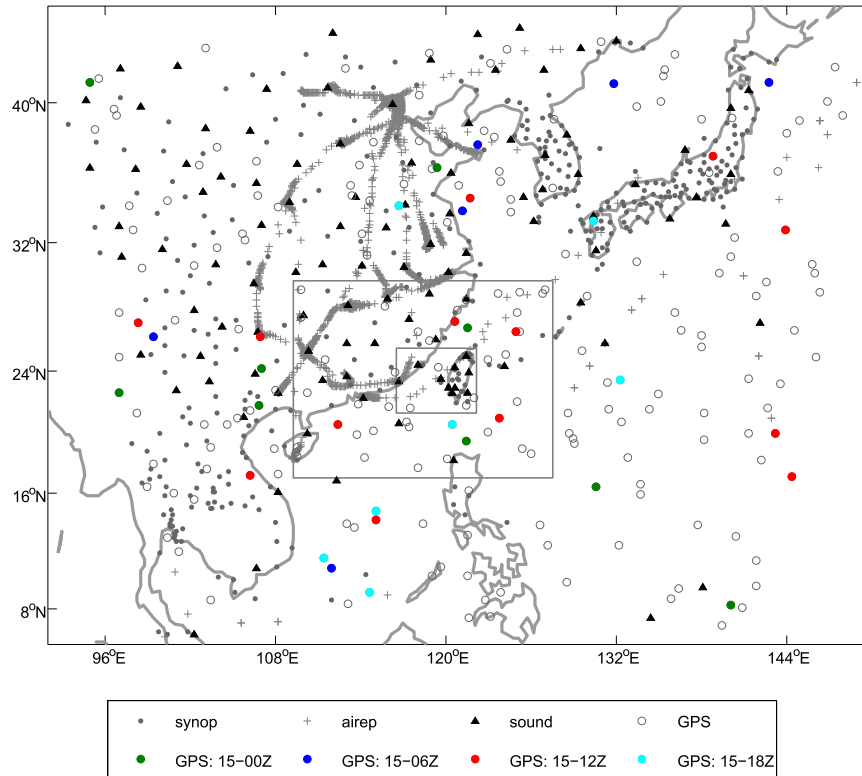


FIG. 3. The WRF Model domain and observations used in the assimilation and forecast experiments. The largest domain with a horizontal grid spacing of 27 km is used for performing the LETKF assimilation. Two additional nested domains (indicated with gray boxes), with horizontal grid spacing of 9 and 3 km, respectively, are included for performing the 30-h forecasts. The color dots denote RO profiles at different times on 15 Jun.

this study include the wind and temperature from rawinsondes, upper-air reports, flight dropsondes, mid- to upper-level satellite winds, surface pressure from the surface stations, and RO refractivity or bending angle from COSMIC (Anthes et al. 2008) using the NCU local bending angle operator. Figure 3 shows all COSMIC observation locations for assimilation and the rest of the observations at 1200 UTC 15 June as a typical distribution. On average, six COSMIC RO profiles in a resolution of about 400 km are available at every analysis time within the model analysis domain. In this study, we also emphasize the impact of the RO data in the analysis of 15 June since the profiles are located in the range of the southwesterly jet, covering and the SCS and Taiwan. The RO data are preprocessed by interpolating the original atmPrf data with a 3-m vertical resolution to a profile with a 100-m vertical resolution.¹ During this

¹ In order to resolve the high moisture in the lower troposphere, the RO data are thinned to have a vertical resolution of 100 m, instead of the model vertical resolution.

SoWMEX IOP period, the rawinsondes in Taiwan are launched every 6 h (Ciesielski et al. 2010), but the flight dropsondes are only available at 0900–1200 UTC 12 June (Davis and Lee 2012). Moisture information from the sounding data is not assimilated on purpose in order to ensure that the observed moisture information is from the RO data.

Table 1 lists the assimilation experiments in this study. The CNTL experiment uses only the conventional observations and satellite winds. Additionally, the BANGLE and REF experiments use the COSMIC RO local bending angle and refractivity, respectively. Through these experiments, we investigate whether the dynamic and thermodynamic features associated with the extreme heavy rainfall events could be represented in the WRF–LETKF analysis and how this may determine the intensity and location of the heavy rainfall event on 16 June. Sensitivity experiments are also performed to validate the impact from the local bending angle; details are further discussed in section 6.

The analysis ensemble means at 1200 UTC 15 June from different experiments are used as initial conditions

TABLE 1. Settings in all the assimilation experiments.

Expt name	Observations	Assimilation impact from bending angle on analysis variables
CNTL	Convention* + satellite wind	
REF	Convention + satellite wind + refractivity	All
BANGLE	Convention + satellite wind + bending angle	All
BANGLE_noWind	As in BANGLE	No direct impact on the wind field
BANGLE_noQv	As in BANGLE	No direct impact on the moisture field
BND2	As in BANGLE, but only assimilate bending angles below 2 km	All
BNDno2	As in BANGLE, but only assimilate bending angles between 2 and 5 km	All

* Convention data used in this study include the sounding from the rawinsondes and flight, upper-air soundings from the air report, and surface station.

for 30-h forecast experiments, which are nested down to 3 km, as shown in Fig. 3. Note that all physical parameterizations used in the assimilation experiments with the 27-km domain are the same for the nested domains in the forecast runs, except that the cumulus parameterization is not activated in the finest (3 km) domain.

5. Results

a. Error covariance and analysis increment in relation to the RO data

In the local RO operator, the model information (temperature T , water vapor mixing ratio Q_v , and pressure P) at one location is used to simulate the refractivity. By further using the information of the vertical gradient of the refractivity, the local bending angle is derived. This leads to different responses from the assimilation of refractivity and bending angle, in addition to the effect of using different observation errors. In this section, we explore the differences of assimilating bending angle and refractivity through the ensemble-based error covariance matrices between the background errors in the observation space and in the model space. This is the same as taking a particular column of the covariance matrix, \mathbf{HP}_f , where \mathbf{H} is the linearized observation operator that maps the model variables to observation space and \mathbf{P}_f is the background error covariance (Kalnay 2003). In the following, the covariance is constructed based on the same moisture field of the background ensemble from the BANGLE experiment at 1200 UTC 15 June covarying with a set of simulated bending angle or refractivity ensemble, given realistic observed RO point data at different heights taken from a COSMIC profile located to the southeast of Taiwan (Fig. 3).

Figures 4a,b are the corresponding covariance structures at the 900-hPa level, constructed with the simulated bending angle and refractivity ensemble, respectively, at 20.9780°N, 123.7630°E and 1 km (point A). At this time

(1200 UTC 15 June), the strong low-level southwesterly conveys high moisture from the SCS to southwestern Taiwan. Difference in the covariance structure is found in this region when the simulated RO observations are located at low levels. Comparing Figs. 4a,b, the characteristics of the background error covariance along line AB is different from the simulated bending angle; nonnegligible covariance ranges from the location of the observation (point A) toward the Bashi Channel. The negative covariance east of 123°E illustrates that this region is out of the boundary of the moisture transport and that the low moisture is affected by the subtropical high. With the vertical cross section along the line AB in Fig. 4a, features with positive covariance in Fig. 5a are mainly present in the boundary layer and negative covariance is shown in the midtroposphere of location A and near 850 hPa over the Bashi Channel. Through this covariance structure, any negative moisture innovations derived with the bending angle at 1 km at location A can increase the moisture above 1 km over the Bashi Channel. In comparison, the covariance associated with the simulated refractivity ensemble at this location has less sensitivity to the moisture gradient and has less response over the Bashi Channel (Fig. 4b). Compared to Fig. 5b, the vertical structure of the covariance is single signed with shallower influence. (Fig. 5b). With an observation at a higher level (3.8 km, near 650 hPa), the \mathbf{HP}_f covariance with the bending angle and refractivity exhibit very similar structures. As shown in Figs. 4c,d, the horizontal structures near the observation level are very similar. Along a direction with weaker moisture gradient (line AC), Figs. 5c,d also show a very similar pattern. This again supports the assumption that the potential benefit from the assimilation of the bending angle comes from the sensitivity to the vertical gradient of the moisture.

The sensitivity of bending angle and refractivity to moisture can be illustrated with the relationship between the ensemble spread and the structure of the moisture

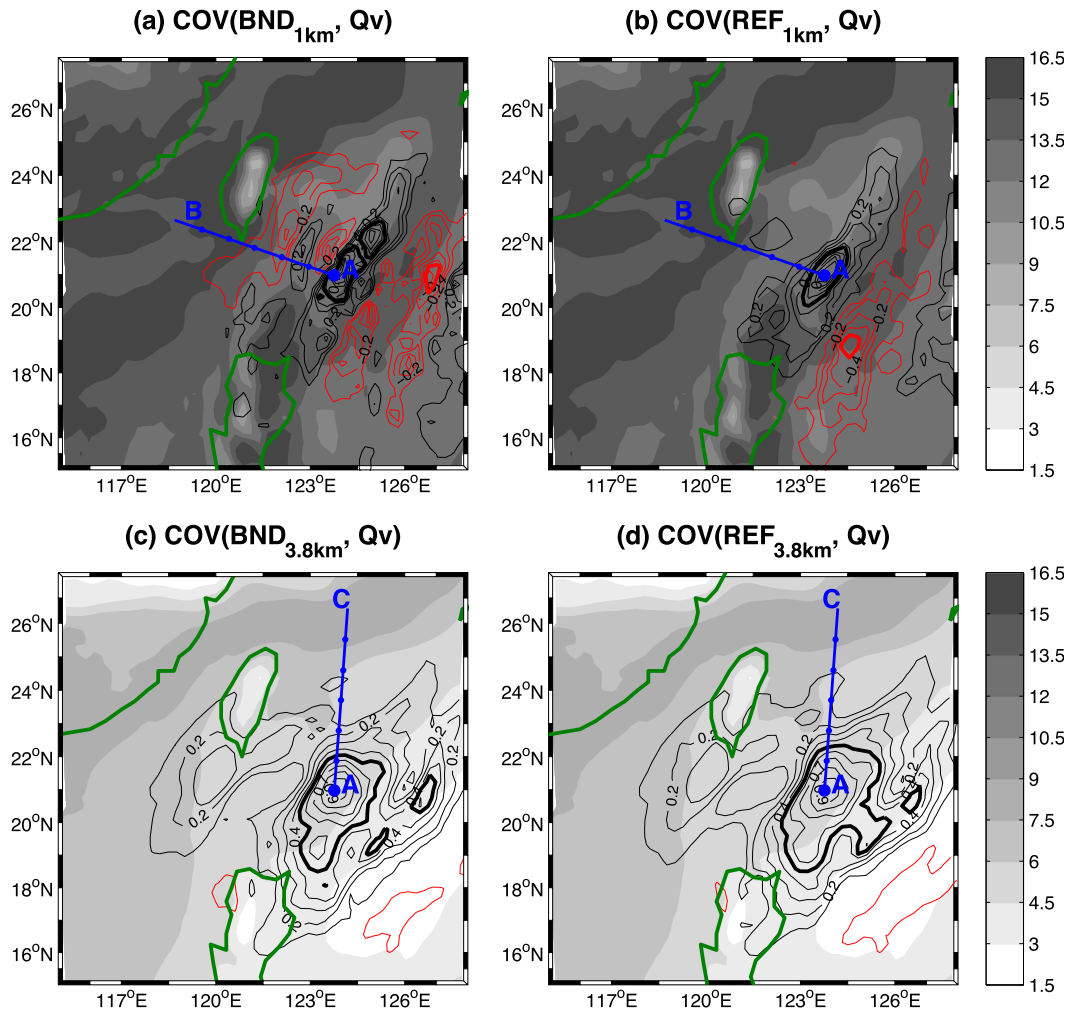


FIG. 4. Ensemble-based covariance between the water vapor mixing ratio at the model level near the 900-hPa level and (a) the bending angle, (b) the refractivity simulated at a COSMIC RO location (point A) at 20.9780°N, 123.7630°E, and 1 km. (c),(d) As in (a),(b), but the RO observation is simulated at 3.8 km and the ensemble of water vapor mixing ratio is near 650 hPa. Red contours denote the negative values. Shading indicates the water vapor mixing ratio (g kg^{-1}). Figures 5a–d use the same ensemble from the background ensemble of the BANGLE experiment at 1200 UTC 15 Jun. Lines AB and AC denote the directions of the cross sections shown in Fig. 5.

field. As shown in Figs. 6a,b, the model state at this observation location is characterized by high moisture and a strong vertical moisture gradient below 1.5 km. Such a characteristic is also reflected in the moisture ensemble, where the large ensemble spread of the moisture can extend toward the level of 3 km but the large spread of the vertical gradient is more concentrated in the low atmosphere below 1 km (Fig. 6d). It is also evident that the spread of the bending angle ensemble captures the characteristics of the vertical gradient of the moisture, showing large spread in the low atmosphere. In comparison, the ensemble spread of the refractivity resembles the behavior of the moisture spread. Results from Fig. 6 suggest that the simulated bending angle ensemble is sensitive to the uncertainties of the moisture gradient in vertical. We also

note that in terms of the fraction, the refractivity spread ($<3\%$) is much smaller than the bending angle spread ($>15\%$ below 1 km). This also justifies the RO observation errors used in this study.

b. Results from the analysis

We first evaluate the general thermodynamic and wind conditions from WRF–LETKF analyses. Figure 7 shows the time–height series of the potential temperature at a model grid point near the Tainan sounding station, located near the coast of southwestern Taiwan (Fig. 1a). The moisture fields do not show much difference at this station among the three experiments during the data assimilation period, except from 1800 UTC 14 June to 0600 UTC 16 June. Especially at 1200 UTC 15

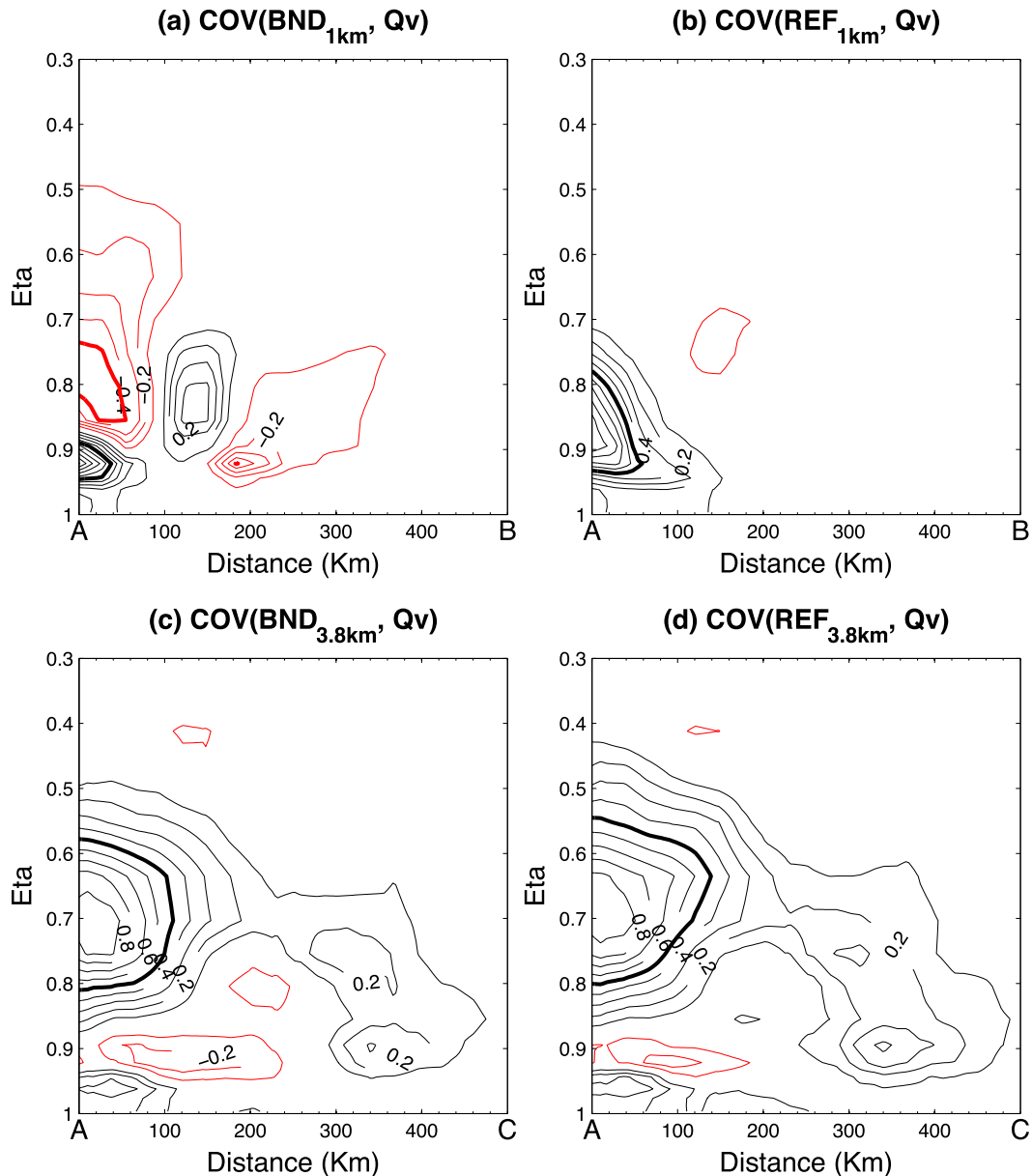


FIG. 5. Vertical cross section of the ensemble-based covariance along lines AB and AC shown in Fig. 4.

June, the convective cloud develops more vigorously (a deeper layer of moisture), in particular from the BANGLE analysis. Also, the REF and BANGLE analyses at this time show moister conditions ($>20 \text{ g kg}^{-1}$) near surface. As for the wind, the southwesterly wind dominates above the 900-hPa levels most of the time in all three analyses, but stronger northward component appears below 950 hPa after 0600 UTC 14 June. The near-surface cooling effect associated with the heavy rainfall is clearly shown during 0000–1200 UTC 16 June (Figs. 7b,c) while such cooling effect is less evident in CNTL (Fig. 7a).

To show the impact from the assimilation of RO data on the amount of moisture, Fig. 8 shows the total precipitable water (TPW) from the background and analyses at 1200 UTC 15 June, when RO profiles are available in the SCS area and the vicinity of Taiwan (see the red dots in Fig. 3). As shown in Figs. 8e,f, the amount of moisture in the SCS area and near Taiwan is significantly enhanced with the assimilation of the RO data. Figure 8f suggests a more profound moisture transport toward southwestern Taiwan via the southwesterly flow. The enhancement of TPW in Fig. 8f is related to the deepening of the moisture layer. Figure 9 compares the

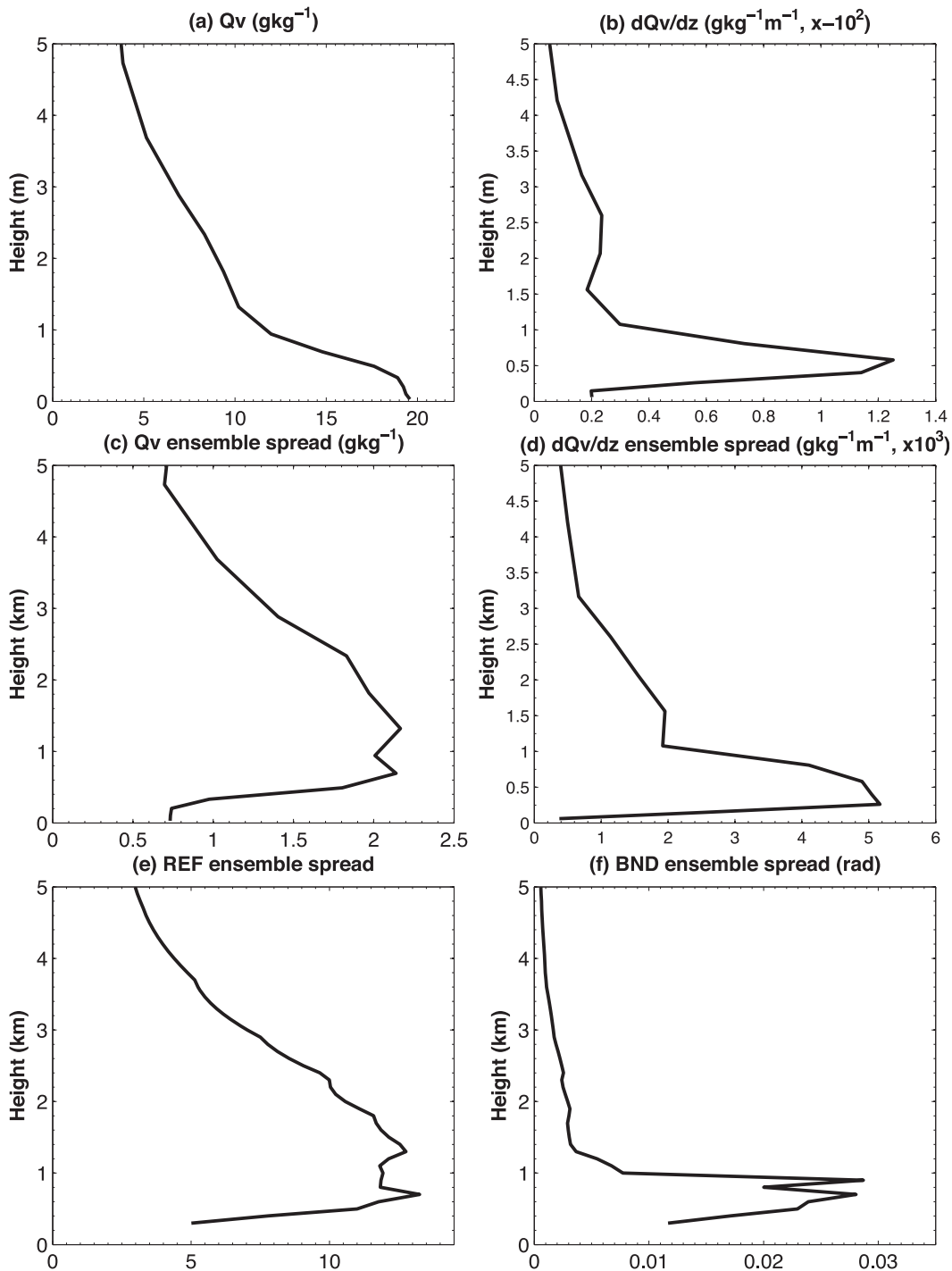


FIG. 6. (a) The ensemble mean state of water vapor mixing ratio and (b) vertical gradient of the mean water vapor mixing ratio at the observation location (20.9780°N, 123.7630°E). Ensemble spread of the (c) water vapor mixing ratio, (d) vertical gradient of the water vapor mixing ratio, (e) refractivity, and (f) bending angle at the same observation location.

moisture profiles derived from the background and analysis at the southwestern part of Taiwan, with the radiosonde observations located at (22.9°N, 120.2°E). For levels above 925 hPa, all backgrounds at this time show drier

conditions. The difference can be as large as $4 g kg^{-1}$ at the level of 700 hPa for the CNTL background. Assimilating refractivity or bending angle provides positive moisture adjustments. But, the assimilation of bending angle

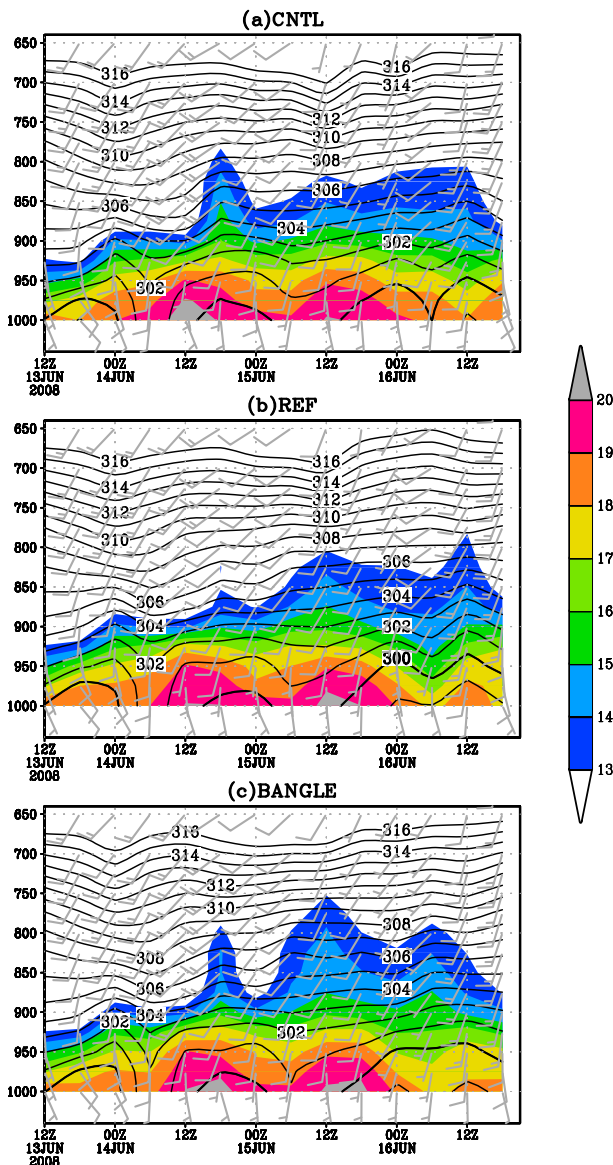


FIG. 7. Time–height series of the potential temperature (contours), water vapor mixing ratio (color shading), and wind barbs at the location of the star in Fig. 1a. A full barb and a half barb represent 5 and 2.5 m s^{-1} , respectively.

improves the moisture at 700 hPa to a level closer to the observation (Fig. 9b). This deeper moisture layer is echoed in Fig. 7c at 1200 UTC 15 June. For comparison, Fig. 9 also shows the moisture profiles derived from the NCEP and ECMWF global analyses, which exhibit very different behavior between 500 and 900 hPa.

At 1800 UTC 15 June, we further compare TPW from the WRF–LETKF analysis with satellite observations [composite of Atmospheric Infrared Sounder (AIRS) and Advanced Microwave Sounding Unit (AMSU)] and global analyses (Fig. 10). Satellite observations (Fig. 10a)

show that relatively high moisture appears in southwestern Taiwan and south of the Guangdong province of China at the SCS (near 20.6°N , 116.6°E). The TPW computed from the BANGLE analysis at this time (Fig. 10d) exhibits a more organized and high moisture region extending from the SCS to the Taiwan Strait. In the REF analysis (Fig. 10c), high moisture occurs over the SCS with a smaller coverage, compared to the BANGLE analysis. Compared to CNTL (Fig. 10b), we note that the local humid regions shown in Figs. 10c,d are meaningful and statistically significant as indicated by the unmasked region. Unfortunately, the ECMWF analysis (Fig. 10e) exhibits a drier condition in the SCS. Although the NCEP analysis (Fig. 10f) is generally moister than the ECMWF analysis in the SCS region, the moist condition does not extend toward southwestern Taiwan at this time. One should keep in mind that these global analyses are regarded as another reference of the nature field. Note that Fig. 10 also illustrates the importance of reflecting the moisture pattern to the mesoscale convection systems in regional analysis; the validation of the local high moisture region in southwestern Taiwan is further justified later based on the precipitation forecasts (section 5c).

Regarding the duration of the heavy precipitation, observations suggest that the low-level convergence is enhanced over the southwestern coast of Taiwan and the adjacent ocean by local convergence related to the local land breeze (Tu et al. 2014). Figure 11 shows the moisture convergence at the 950-hPa level at 1200 UTC 15 June. All three experiments show nice moisture convergence off the southwestern coast of Taiwan. The initial condition is set up for heavy rainfall starting offshore and propagating toward Taiwan. Compared to CNTL, the convergence zones from REF and BANGLE extend farther southwest toward the ocean.

When the GPS RO data are assimilated, the strength of the southwesterly is slightly decreased at low levels. However the westerly component between 22° and 23°N to the southwest of Taiwan is increased (Figs. 11b,c). This modifies the wind direction more toward inland and improves the rainfall forecast extending toward the coastal region of southwestern Taiwan, as will be discussed in section 5c.

c. Impact on the forecast initialized at 1200 UTC 15 June 2008

With the analysis discussed above, the heavy rainfall on 16 June can only be reasonably captured with the BANGLE analysis after 1200 UTC 15 June. In comparison, the number and location of the RO profiles at 0000 and 0600 UTC (Fig. 3) may not be able to have a significant impact on the heavy precipitation over

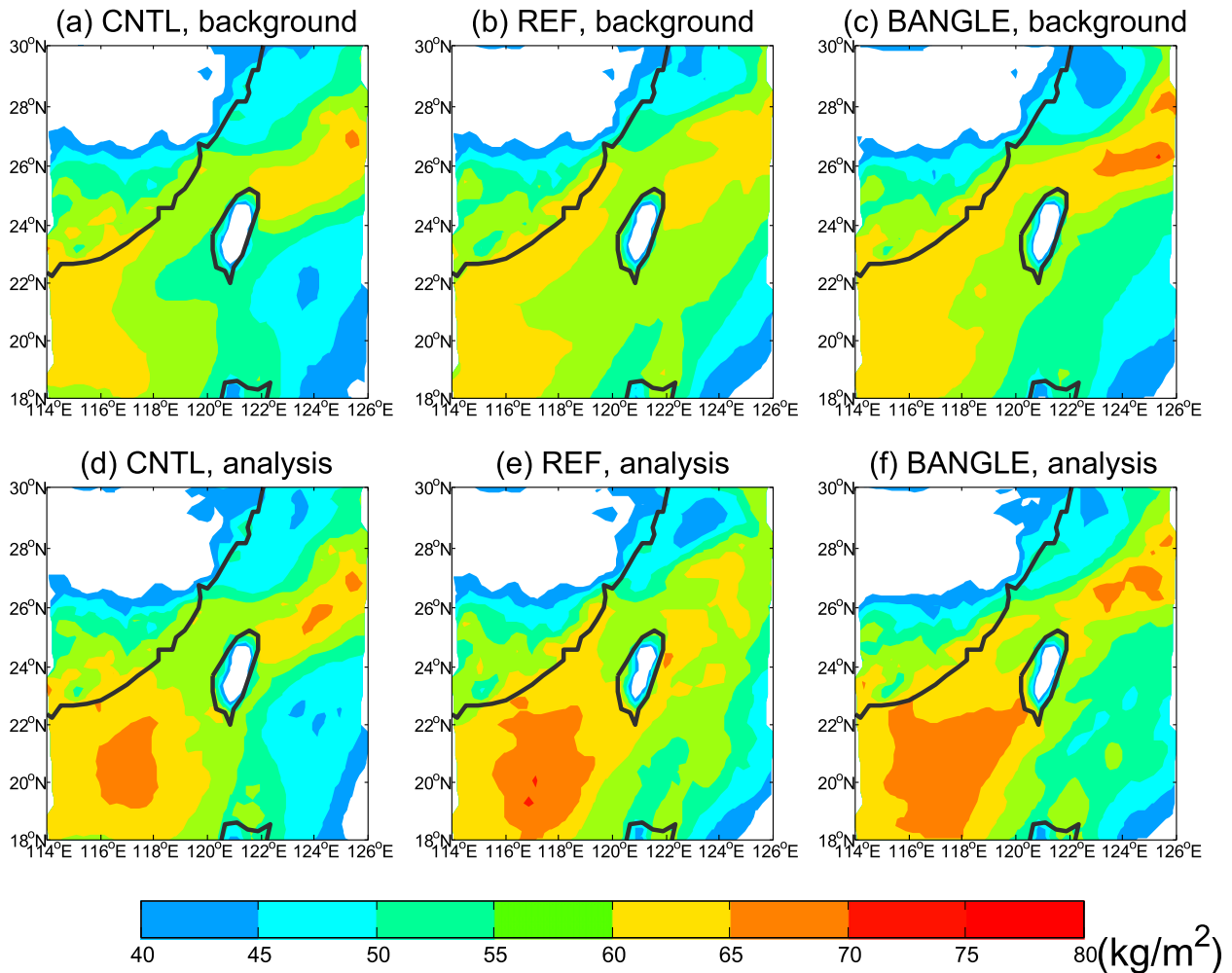


FIG. 8. TPW (kg m^{-2}) from (top) the background and (bottom) analysis at 1200 UTC 15 Jun 2008 from the (a),(d) CNTL; (b),(e) REF; and (c),(f) BANGLE experiments.

southwestern Taiwan. After 1200 UTC, RO profiles are not only available around Taiwan, but are also located at the upstream of the moisture transport (i.e., the SCS region).

Initialized at 1200 UTC 15 June 2008, the accumulated rainfall prediction on 16 June is shown in Figs. 12a–c. The CNTL forecast shows that the heavily precipitated area is limited in the southern part of Taiwan. When the COSMIC RO data are assimilated, both the location and intensity of the heavy precipitation over southwestern Taiwan are improved, especially for the rainfall amount greater than 50 mm day^{-1} (Figs. 12b,c). Compared to observations (Fig. 1b), the location and intensity of the precipitation are better captured after the assimilation of GPS RO data and are slightly better with the use of bending angle than with the use of refractivity, especially for improving the heavy rain in the southwest part of Taiwan.

The forecast skill of the equitable threat score (ETS) and bias scores are computed based on the accumulated rainfall prediction on 16 June in Taiwan. Results show that the ETS and bias scores from the BANGLE forecast are significantly higher than the other two forecasts for thresholds larger than 100 mm day^{-1} , as listed in Table 2. This suggests that the bending angle data are beneficial for predicting the location and intensity of the heavy rain in this event. Although the REF forecast also shows high bias scores, the ETS scores are relatively low for thresholds larger than 100 mm day^{-1} , because much of the heavy rain falls in the southern Taiwan.

In addition to the deterministic forecasts initialized from the analysis mean, results from ensemble forecasts also suggest that the ensemble incorporated with the impact from the RO bending angle has a better chance to capture the heavy rainfall. Figure 13 shows the probability quantitative precipitation forecast (PQPF) computed from the

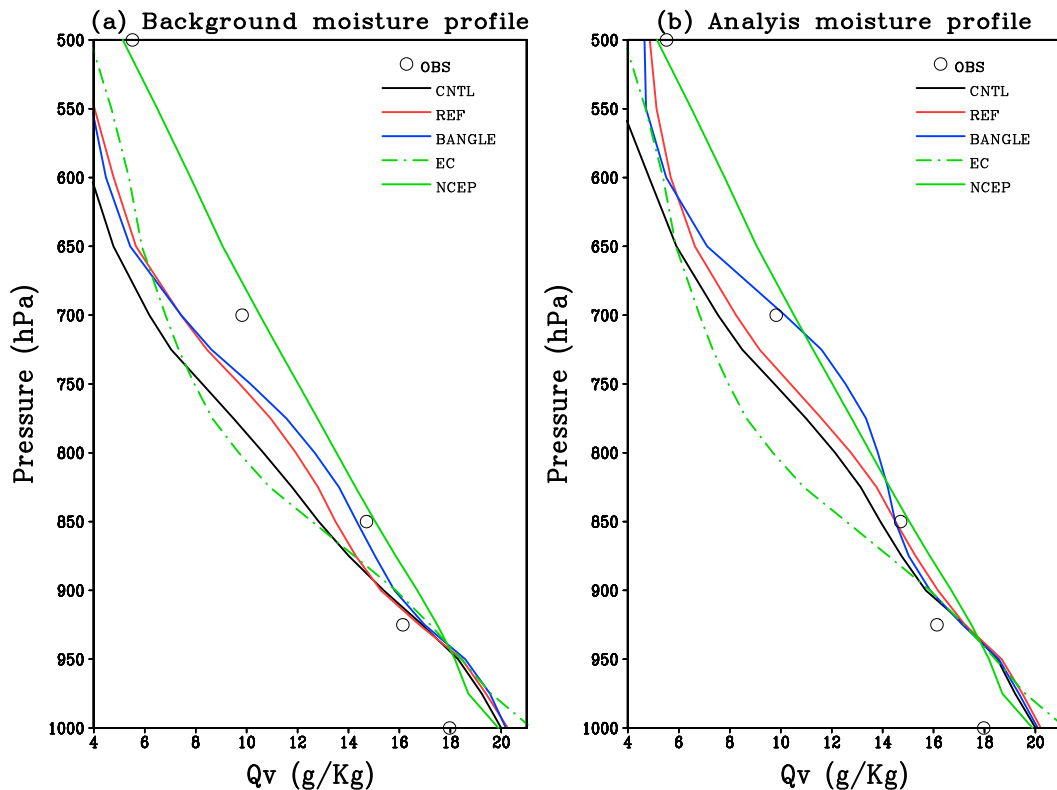


FIG. 9. Moisture profile averaged over $0.5^\circ \times 0.5^\circ$ domain centered at $(23.0^\circ\text{N}, 120.2^\circ\text{E})$ from (a) background and (b) analysis at 1200 UTC 15 Jun. The green solid and dashed lines are derived from the NCEP FNL ($0.5^\circ \times 0.5^\circ$) and ECMWF ($0.25^\circ \times 0.25^\circ$) global analyses, respectively. Dots denote radiosonde observations located at $(22.9^\circ\text{N}, 120.2^\circ\text{E})$.

ensemble forecasts initialized from CNTL, REF, and BANGLE analysis ensemble at 1200 UTC 15 June. With a threshold of 50 mm day^{-1} (the definition of heavy rainfall used in Central Weather Bureau in Taiwan), the PQPF from the CNTL ensemble forecast is lower and mostly is located south of 22.6°N (Fig. 13a), while the observed heavy rainfall appears north of 22.6°N (Fig. 1b). On the other hand, Figs. 13b,c show that both BANGLE and REF ensemble forecasts can capture heavy rainfall in the coastal region of southwestern Taiwan with a comparable probability. However, REF ensemble forecast predicts a higher probability of heavy rainfall over southern Taiwan that was not shown in observation (Fig. 1b). Therefore, Fig. 13c suggests that analysis ensemble incorporated with the RO bending angle provides a higher potential condition for generating heavy rainfall near southwestern Taiwan in this case study.

The differences in the initial conditions (the analyses discussed in section 5b) show that when the bending angle is assimilated, the westerly component between 22° and 23°N to the southwestern of Taiwan is increased (Figs. 11b,c). This modifies the wind direction and moisture transport more toward inland and facilitates the

development of the heavy precipitation. In addition, the duration of the heavy rainfall is related to the maintenance of the convergence zone. As shown in Figs. 11b,c, the extension of the moisture convergence from offshore to coastal region of southwestern Taiwan enables both REF and BANGLE forecast to have a longer heavy rainfall period.

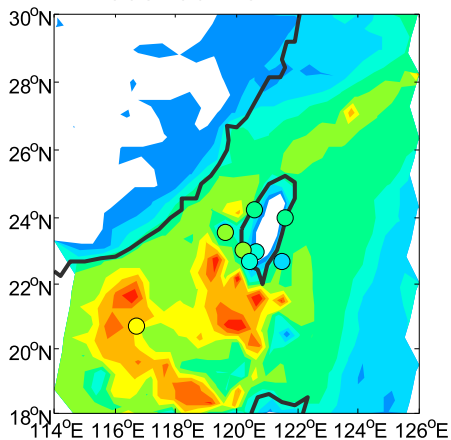
We also note that forecasts initialized from BANGLE and REF analyses at 1800 UTC 15 June consistently show a better rainfall forecast than the CNTL forecast (Figs. 12d–f). The improvement from REF is even more evident.

In short summary, the GPS RO data have the benefits of representing the important elements, in terms of the dynamic and thermodynamic states, for reproducing the heavy precipitation event on 16 June.

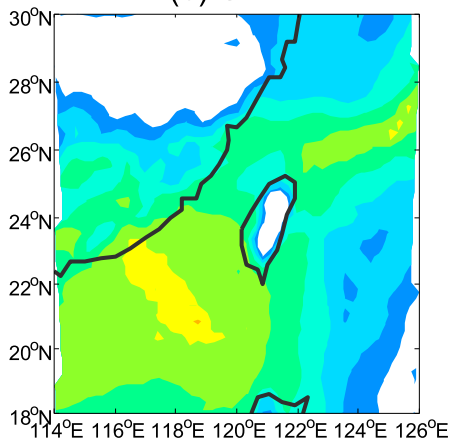
d. The impact from the bending angle on the moisture and wind fields

In this subsection, we investigate how assimilating the bending angle can affect the moisture transport, which is related to both moisture and horizontal wind fields. We performed two assimilation experiments to turn off the impact of the bending angle on the wind or moisture

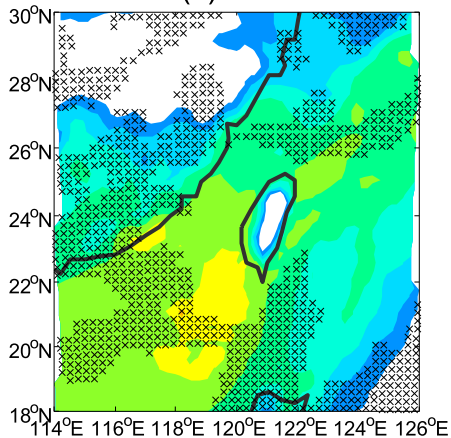
(a) AIRS+AMSU, totH2OMWOnlyStd,
2008-06-15-17:42 Z



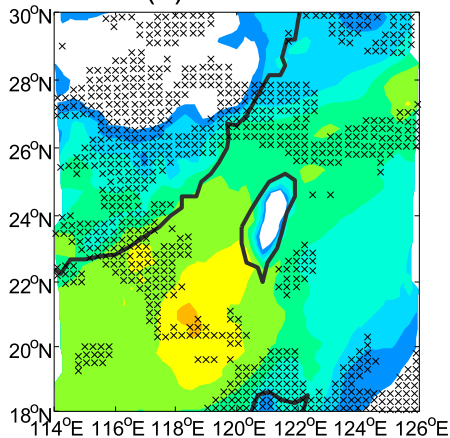
(b) CNTL



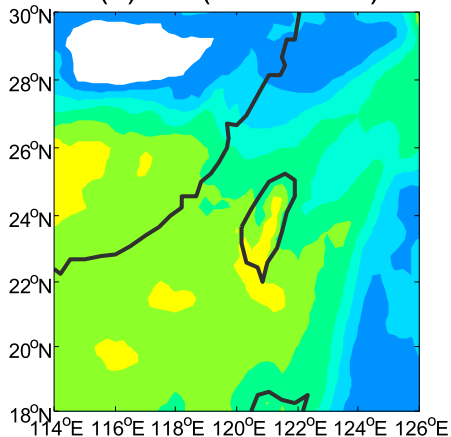
(c) REF



(d) BANGLE



(e) EC (0.25° x 0.25°)



(f) NCEP FNL (1° x 1°)

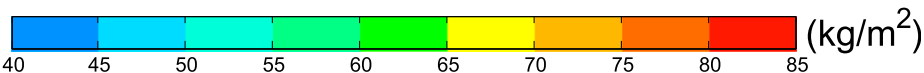
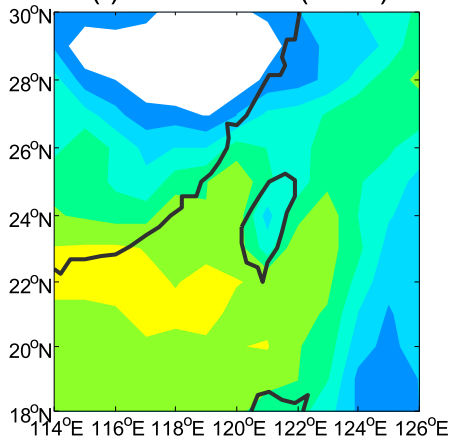


FIG. 10. TPW in color scale from (a) the observation of AIRS and AMSU data at 1742 UTC 15 Jun and sounding data (scattered circles) at 1800 UTC, and from the WRF-LETKF analysis of (b) CNTL, (c) REF, and (d) BANGLE analyses at 1800 UTC 15 Jun. The (e) ECMWF (0.25° × 0.25°) and (f) NCEP (0.5° × 0.5°) global analyses at the same time. In (c) and (d), the areas not masked with crosses denote that the TPW is significantly greater than the one derived from CNTL.

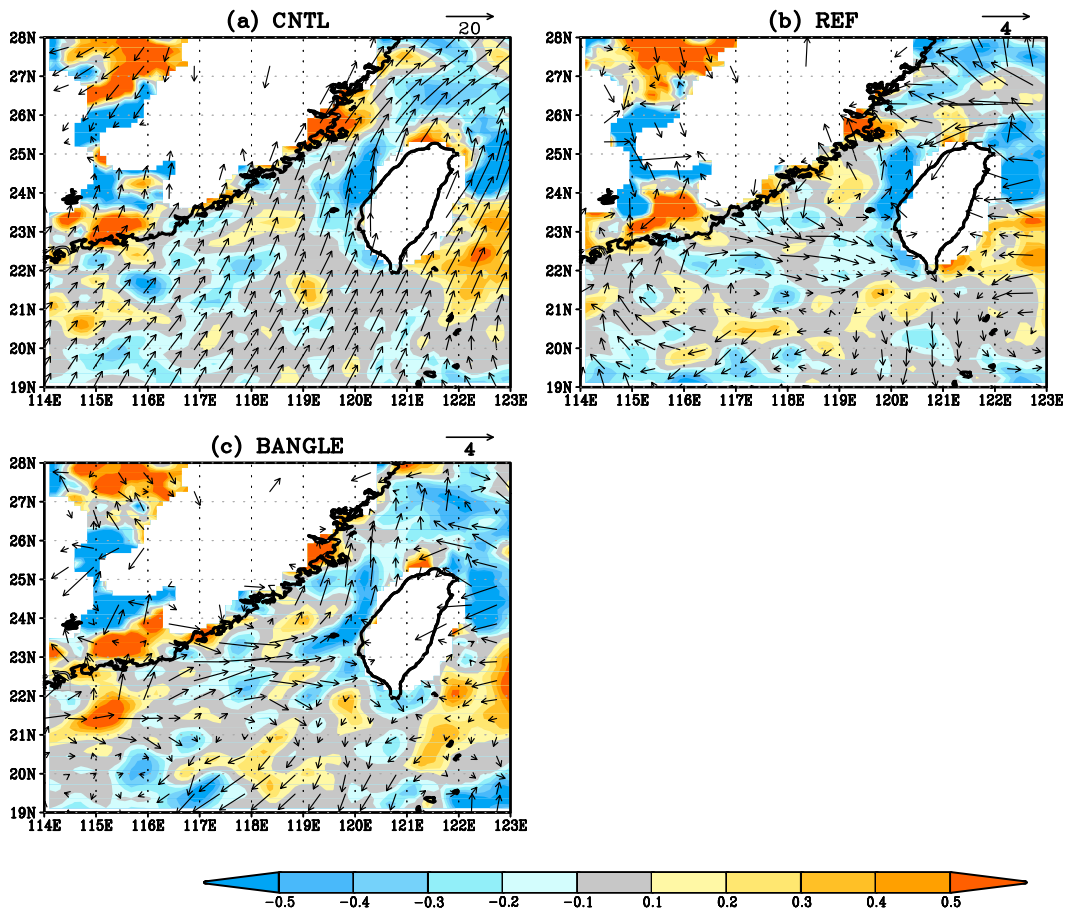


FIG. 11. Moisture convergence at the 950-hPa level from the (a) CNTL, (b) REF, and (c) BANGLE analysis at 1200 UTC 15 Jun. The arrows shown in (a) indicate the CNTL wind field. The arrows shown in (b) and (c) indicate the wind analysis differences between REF and CNTL and between the BANGLE and CNTL, respectively.

field during the LETKF analysis step. They are referred to as BANGLE_NoWind and BANGLE_NoQv, respectively. Unlike the experiments discussed in previous sections, both experiments start from the BANGLE background ensemble at 0000 UTC 15 June with three cycling runs until 1200 UTC 15 June.

Figure 14 shows the 950-hPa water vapor mixing ratio (color shading) and convergence (black lines) of the analyses at 1200 UTC 15 June. In Fig. 14a, it is evident that high moisture and strong convergence surround Taiwan, which leads to the heavy precipitation on 16 June. When the bending angle has no impact on the wind field at the analysis steps, features that contribute to heavy rainfall can still be presented. However, such features cannot be obtained when the bending angle has no impact on the moisture field. Such moisture differences between the BND_noWind and BND_noQv are still significant until 3 km in the coastal region of southwestern Taiwan. This confirms that the main effect from the bending angle is on the moisture field in that

area. Compared to Fig. 14b, the weaker convergence in Figs. 14a,c may suggest the assimilation of bending angle may have slightly degraded the wind fields in this case. Since the wind variable is not directly related to the bending angle, the corrections on the wind field depends on the robustness of the cross-variable covariance between model wind and simulated bending angle. At this time, the enhancement on the convergence field shown in Fig. 14b is mainly due to model dynamics and the assimilation of the sounding near Taiwan.

6. Results from sensitivity experiments

a. The importance of bending angles at different heights

To test the forecast sensitivity to the bending angle and its associated impact on the moisture field and precipitation prediction, we performed two experiments as listed in Table 1. These experiments use the same setup as the BANGLE experiments, except that different levels of

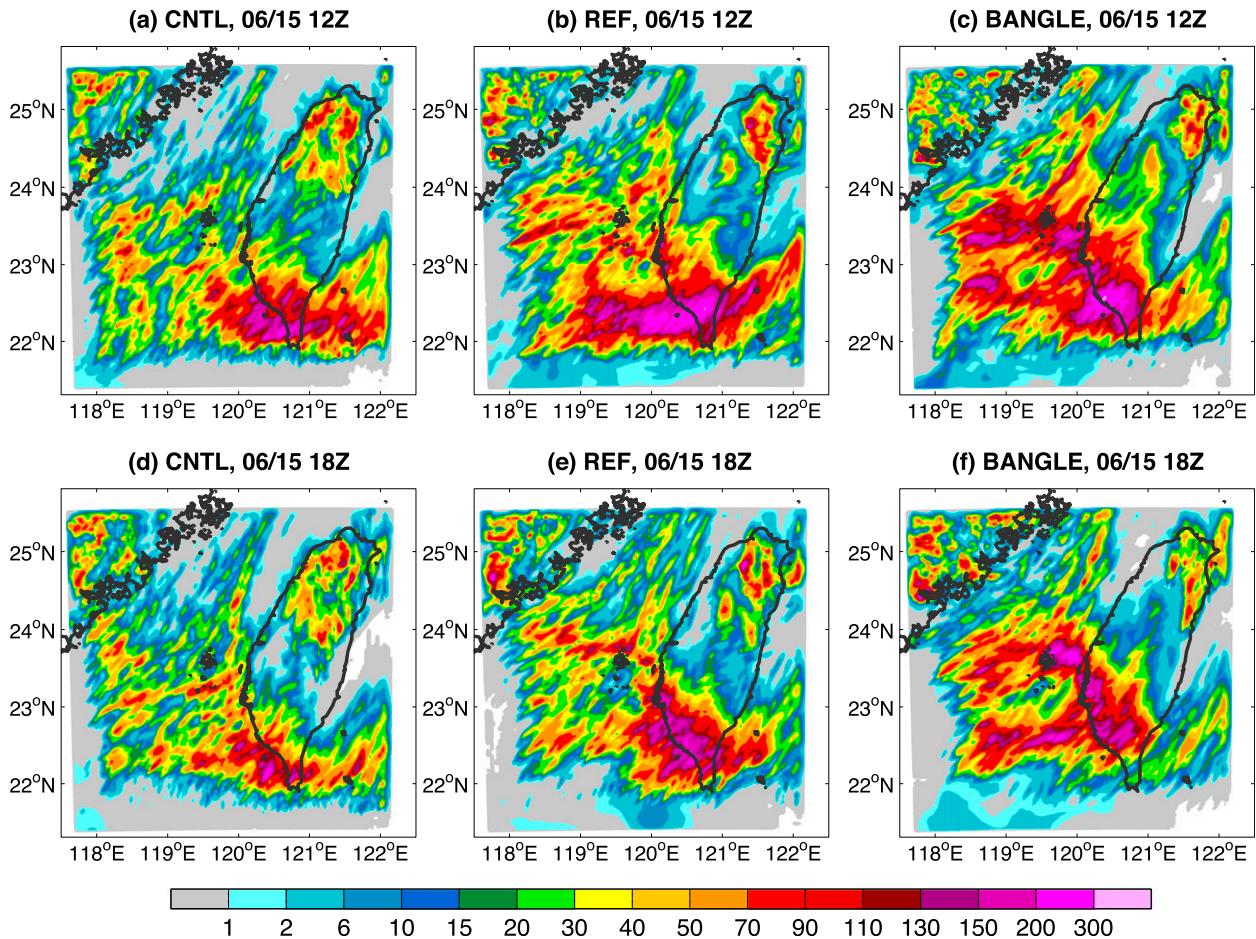


FIG. 12. Total precipitation in color scale (mm) on 16 Jun (accumulated from 1600 UTC 15 Jun to 1600 UTC 16 Jun) from the forecasts initialized from (a) CNTL, (b) REF, and (c) BANGLE analyses at 1200 UTC 15 Jun. (d)–(f) As in (a)–(c), but the forecasts are initialized at 1800 UTC 15 Jun.

bending angle observations are assimilated. Bending angles below 2 km are assimilated in the BND2 experiment, while the BNDno2 experiment assimilates bending angle between 2 and 5 km.

Figure 15 shows the mean moisture difference between the RO data-related analysis and the CNTL analysis and the difference is averaged based on a box near southwestern Taiwan (20°–22.5°N, 117°–120.5°E) at 1200 UTC 15 June. First, it is clear that assimilating bending angle greatly increases the moisture amount between 850 and 500 hPa. Although BND2 shows that assimilating the bending angles below 2 km indeed helps to increase the moisture amount below 900 hPa, the moisture content above 900 hPa is significantly smaller than the BANGLE analysis. When assimilating bending angle above 2 km, the midlevel atmosphere becomes moister again.

As expected, the moisture differences shown on Fig. 15 have a great influence on the rainfall prediction. Forecast results (figures not shown) indicate that BNDno2 exhibits

a greater rainfall amount in southwestern Taiwan than BND2 does. This suggests that the bending angle between 2 and 5 km plays an important role in deepening the moist air in the SCS and southwestern Taiwan, and with the low-level convergence, the moisture transport toward southwestern Taiwan can be further enhanced.

TABLE 2. (top) ETS and (bottom) bias of the quantitative precipitation forecast on southwestern Taiwan on 16 Jun.

Observation	Threshold (mm day ⁻¹)		
	50	100	130
ETS			
CNTL	0.19	0.10	0.03
Bending angle	0.45	0.52	0.39
Refractivity	0.46	0.11	0.10
Bias			
CNTL	0.92	0.39	0.33
Bending angle	1.33	0.79	0.75
Refractivity	1.07	0.56	0.32

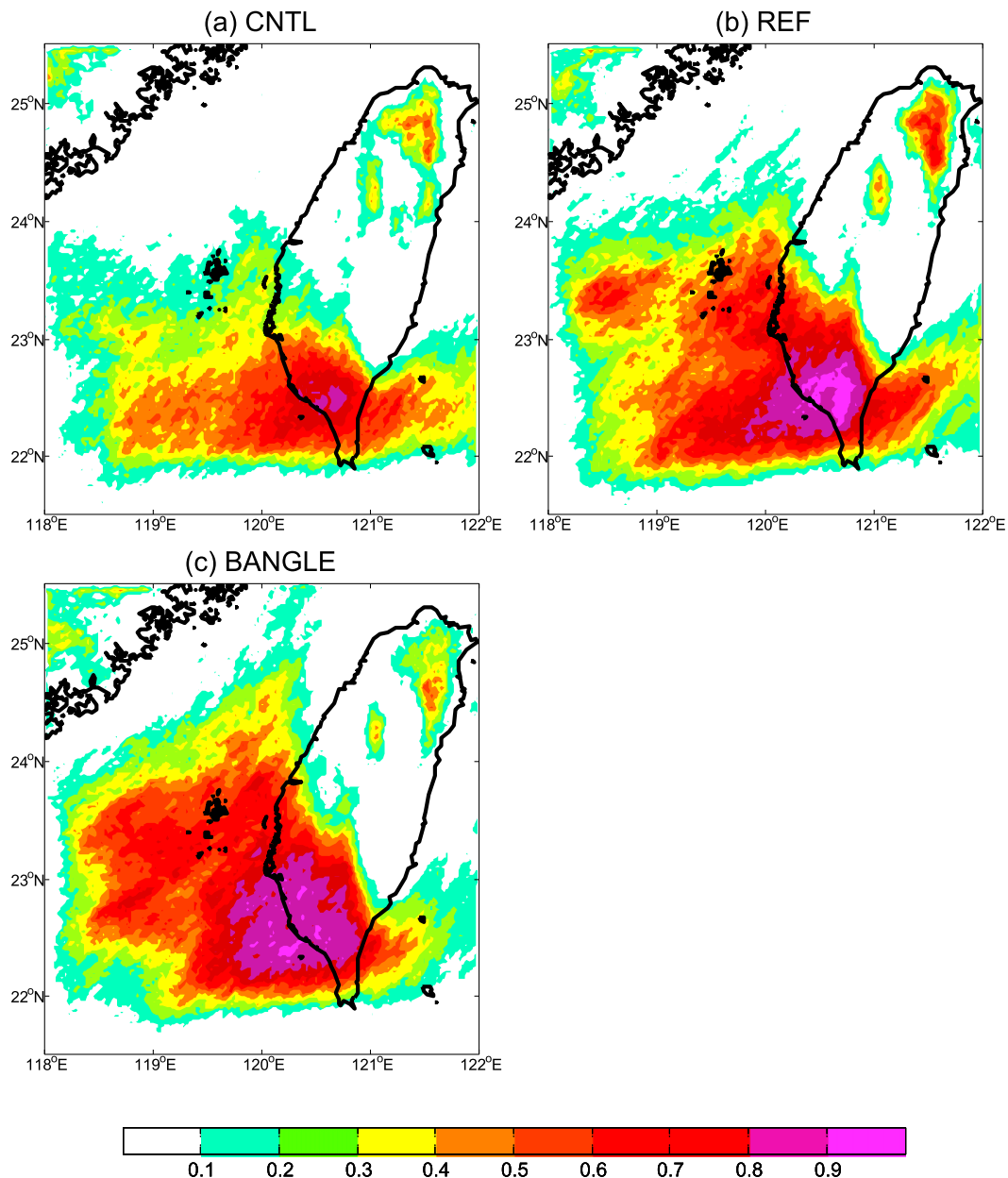


FIG. 13. Probability quantitative precipitation forecast (PQPF) with a criteria of 50 mm day^{-1} on 16 Jun (accumulated from 1600 UTC 15 Jun to 1600 UTC 16 Jun) from the ensemble forecasts initialized from (a) CNTL, (b) REF, and (c) BANGLE analysis ensemble at 1200 UTC 15 Jun.

b. Uncertainty in the bending angle operator

As discussed in section 3b, contribution from the bending angle above the model top follows the method in Healy and Thépaut (2006), with extrapolation by assuming that the refractivity decays exponentially above the model top. The bending angle above the model top may introduce some uncertainty during the calculation within the model domain and a lower model top might introduce a larger error. Although the

uncertainties associated with the choice of model top are accumulated and affect lower levels through integration, such accumulated error is relatively small compared to low levels where most moisture resides. Based on the innovation statistics, the error of the bending angle at the model top is about 2.85% of the observation, which is not assimilated in this study. Such an error attributes 0.71% and 0.46% of errors at 5 and 1 km, respectively, and are also much smaller than the observation error.

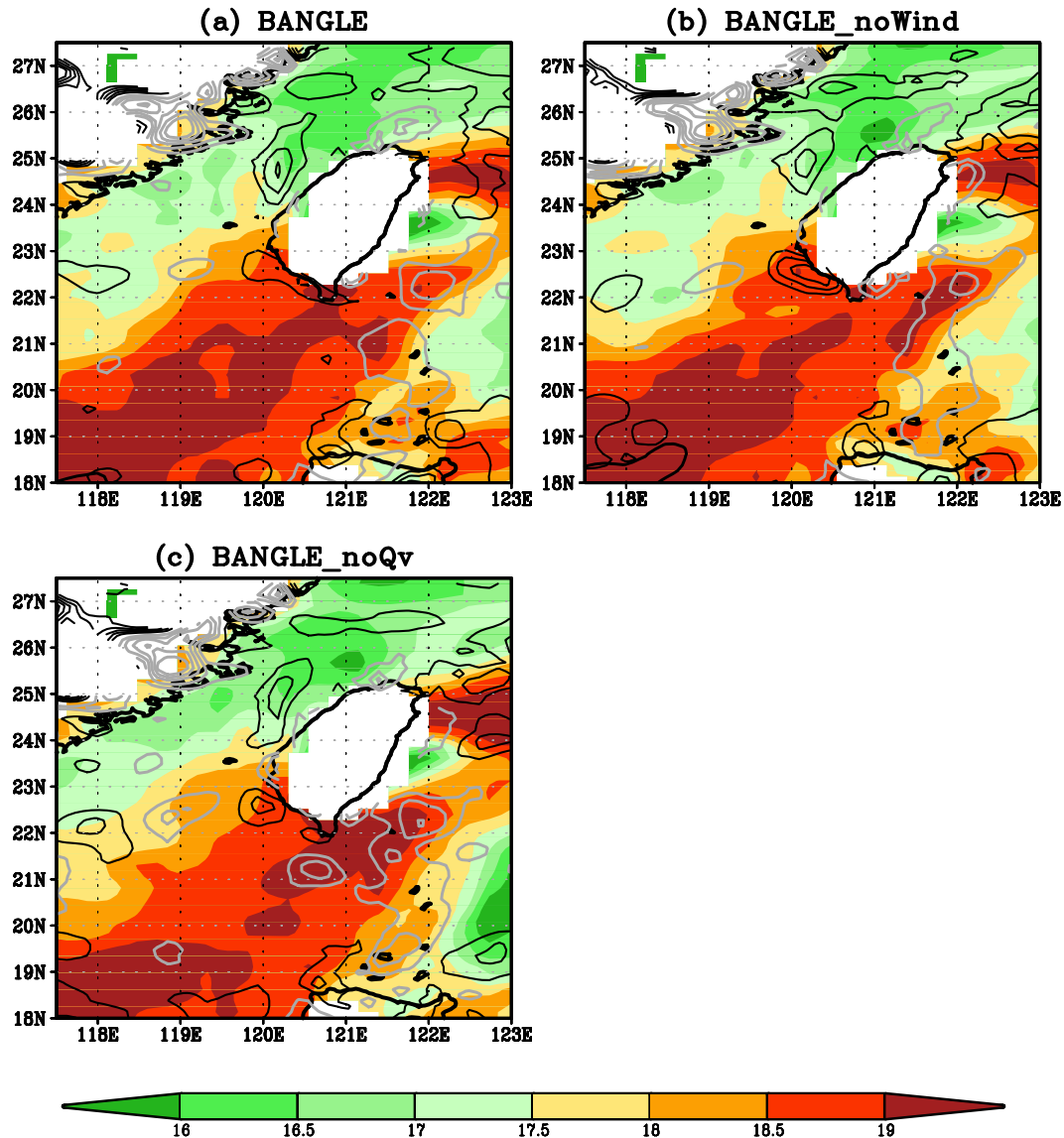


FIG. 14. 950-hPa water vapor mixing rate (color shading) and convergence (black contours) from analyses at 1200 UTC 15 Jun with RO bending angle assimilated. The bending angle has (a) full effect, (b) no impact on updating the wind fields, and (c) no impact on the moisture field. Divergence is denoted in gray contours.

It is inevitable that the model top of WRF, or other regional models, is much lower than that which has been used in global models. Under this situation, the extrapolation from the model top may not be adequate for regional models and should be further studied. While this study does not intend to answer this question, we have conducted two more sensitivity experiments to assess the impact of the bending angle uncertainties, contributed to by the assumption of bending angles above the model top. As we demonstrate in the following, such uncertainties have some impact on analysis, but are small enough to be neglected when assimilating bending angles below 5 km, as in this study.

In the default experiment, the bending angle above the model top, named *bdarm*, follows Healy and Thépaut (2006) (Fig. 16a). It uses the BANGLE background at 1200 UTC 15 August and assimilates only the RO bending angle data. The issue of the error contributed by a lower model top height is assessed by reducing (Fig. 16b) or increasing (Fig. 16c) 10% of the bending angles of that from *bdarm* above the model top. Note that the innovations of the local bending angle at the top of the model vary about from -7% to 7% , and therefore, the 10% is chosen for these *bdarm* sensitivity tests. The assessment is evaluated by the increment of the total precipitable water vapor. As shown in Fig. 16, the uncertainty associated with the model

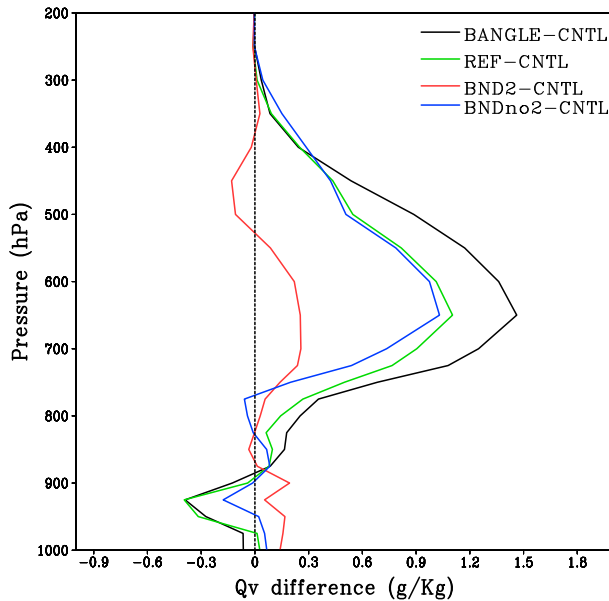


FIG. 15. Mean difference in water vapor mixing ratio between the RO data associated and CNTL analyses. The difference is averaged based on an area near southwestern Taiwan (20° – 22.5° N, 117° – 120.5° E).

top has a small impact on the increments. These increments are the same in signs and the differences among them are small. As expected, these tiny differences do not induce significant difference in the location and intensity of the rainfall prediction. However, we should note that such conclusion may only apply when assimilating bending angles at a lower atmosphere (i.e., 5 km in this study). For the purpose of this study, we emphasize the RO impact on the moisture field. The local operator should be further evaluated to simulate bending angles at higher levels, where the bending angle is one order smaller than that at the low atmosphere.

7. Conclusions

GPS-RO data have been broadly used in global and regional numerical weather predictions. Although assimilation with the bending angle often performs better than refractivity in many studies of global prediction (e.g., Healy and Thépaut 2006; Cucurull et al. 2007), a study furnishing the feasibility of bending-angle assimilation in the prediction of regional heavy precipitation systems is appealing. The local RO operators for simulating bending angle and refractivity are implemented in the WRF-LETKF framework to evaluate the impacts of these two types of COSMIC RO data on the prediction of a heavy precipitation episode during SoWMEX-IOP8 in 2008. With the WRF-LETKF analyses, we investigate what the primary

elements are in the initial conditions for predicting the intensity and location of the heavy precipitation and how the assimilation of RO data can contribute.

The difference between the assimilation of the refractivity and the bending angle data is examined by the structure of the ensemble-based \mathbf{HP}_f error covariance, between the background state in the observation space and in the model space. Results suggest that assimilation of bending angle can lead to analysis corrections more sensitive to the vertical gradient of the moisture, especially in the low troposphere. Similar structures of the \mathbf{HP}_f error covariance are obtained with either the refractivity or the bending angle located at higher levels and in the region with a small moisture content and a weak vertical moisture gradient; and thus similar patterns of analysis correction are expected.

Based on the WRF-LETKF analyses, results suggest that positive influences are obtained with the COSMIC RO data by improving the moisture field. Particularly, the impact of the COSMIC RO bending angle is shown in deepening the depth of moist air and affecting the thermodynamic variables. Overall, the analysis incorporated with the bending angle (BANGLE) shows an enhanced moisture transport with a deeper layer of moisture in the SCS and offshore southwestern Taiwan. As a result, this creates a more favorable condition for generating heavy precipitation in the coastal region of southwestern Taiwan on 16 June.

Forecasts initialized after 1200 UTC 15 June suggest that for this particular case study the COSMIC-RO bending angle has a significant impact on improving the heavy precipitation forecast. Without the COSMIC-RO data, the analysis shows a drier condition in the coastal area of southwestern Taiwan and the convergence is more confined to the coastal area. As a result, the intensity of rainfall forecast in Taiwan is not strong enough and the location is farther southward, compared to the observation. With the COSMIC-RO data, the location of the heavy rainfall is improved and extended toward the coastal region of southwestern Taiwan as seen in the observations. By assimilating the bending angle, the high moisture region offshore southwestern Taiwan is well depicted with the support of the local convergence extending from coastal to offshore southwestern Taiwan, and consequently, the location and intensity of precipitation can be better predicted than the one derived from the CNTL forecast. With similar patterns of moisture enhancement, the REF analysis, however, is not as moist as the BANGLE analysis between 700 and 900 hPa and the rainfall prediction is slightly worse in terms of the location of the heavy rainfall based on the ETS forecast score. In addition to the deterministic forecasts, the PQPF also suggests that the impact from the RO bending

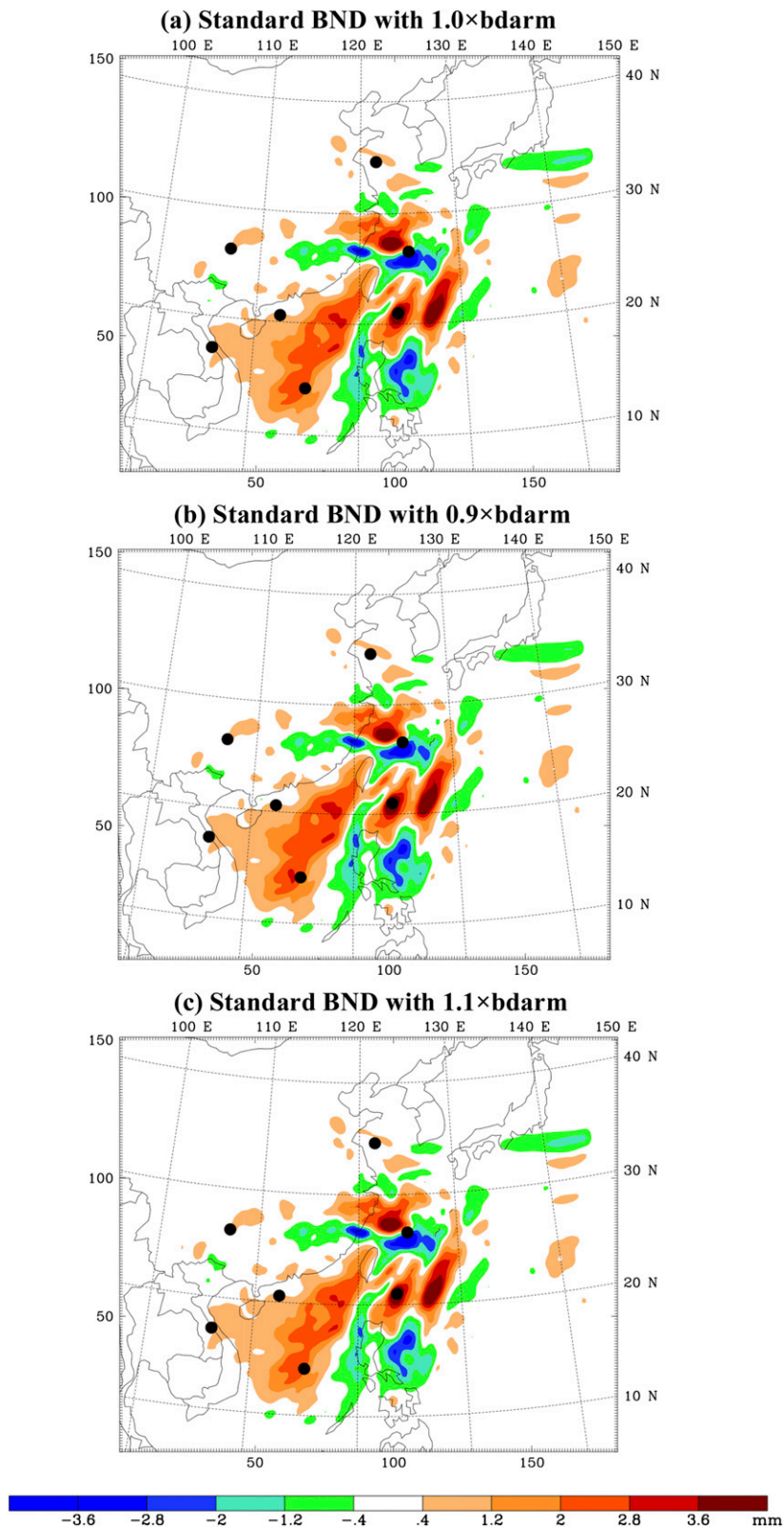


FIG. 16. The increment of total precipitable water vapor (mm) after modifying the calculation of bending angle above the model top with a factor of (a) 1.0, (b) 0.9, and (c) 1.1 times.

angle indeed leads to a better probability distribution for the location of the heavy rainfall.

Through the sensitivity experiments, we conclude that for this case study the importance of the bending angles is to deepen the moist air in the SCS and southwest of Taiwan. Only when the moist air is deep enough, can the intensity of the rainfall be successfully depicted with the help of the convergence offshore southwestern Taiwan.

When initializing the forecasts at 1800 UTC 15 June, the BANGLE and REF forecasts both show a consistent performance and improvement over southwestern Taiwan. Given that the impact of the RO profile depends on its relative location to the event of interest, future studies with the much densely distributed RO data (COSMIC-II) can further confirm its impact on the regional severe weather prediction.

In this study, we show the positive impact of assimilating COSMIC RO bending angles on heavy rainfall prediction over Taiwan with low-level limited (below 5 km), available RO soundings using the WRF-LETKF system. In comparison to the local refractivity operator, the local bending angle operator performs slightly better because it can deepen the depth of moisture layer, which is essential for successfully delivering the severe weather prediction. The role of RO data at higher altitudes (above 5 km) is not investigated in this study because the regional model uses a model top usually much lower than the global models. Although the uncertainties associated with the assumption of the bending angle above the model top contribute a relatively small amount of error for simulating the bending angle at the low level, the simulation of RO bending angle may contain larger errors at higher altitude with a model top of 50 hPa. This may introduce faulty observation innovations (the maximum about 7% in this study) and mislead analysis corrections, which can be magnified by the use of small observational errors at upper levels (e.g., 1% at 10 km). Also, the description of the observation error variance at upper levels needs to be properly estimated, since the bending angle at the upper level becomes much smaller at upper levels. In this study, we just follow the specification of bending angle observation errors in global models (Healy and Thépaut 2006). With operational global models, Healy et al. (2007), Healy (2008), and Cucurull et al. (2013) have confirmed that the assimilation of RO data with entire vertical range can improve the temperature forecast in the upper troposphere and lower stratosphere. In the future, a combination of both bending angle and refractivity assimilations for different vertical ranges may turn out to be a better strategy for regional models for taking full advantage of the RO data.

Acknowledgments. The authors are very grateful to Dr. Y.-H. Kuo from NCAR and Dr. Healy from ECMWF for valuable discussions and suggestions, and to three anonymous reviewers for improving the manuscript. The authors are also thankful to Mr. Cheng-Chieh Kao and Ms. Ai-Lin Hsao for technical support. The authors would like acknowledge the NSPO-TACC and EUMETSTAT for providing the RO data and the SoWMEX/TiMREX team for providing valuable observations for assimilation and comparison. This work is sponsored by the National Space Organization Grants NSPO-S-099010 and NSPO-S-101011, and is partially supported by the U.S. National Science Foundation Award 100602-200912528. Shu-Ya Chen is sponsored by the National Science Foundation Grant AGS-1033112.

APPENDIX

A Local Operator for the RO Bending Angle

A local bending angle operator has been developed at the National Central University (NCU), Taiwan (Chen et al. 2010), and implemented into the WRF-LETKF system.

An Abel transform is applied to this operator in order to inverse the model's local refractivity profile to the "local" bending angle. Here, local means using the model local refractivity value at the occultation column, instead of the actual value following the ray by solving the ray-tracing equation, under the assumption of local symmetry. Following Kursinski et al. (1997), the observation operator is constructed to evaluate the bending angle integral given the observed impact parameter a :

$$\alpha(a) = -2a \int_a^{\infty} \frac{d(\ln n)/dx}{\sqrt{(x^2 - a^2)}} dx, \quad x = nr, \quad (\text{A1})$$

where α is the bending angle, n is the refractive index derived from the model, and r is the radius value of a point on the ray path. And the atmospheric refractivity, defined as $N = (n - 1) \times 10^6$, varies with the atmospheric pressure, temperature, and the moisture. It can be calculated by

$$N = 77.6 \frac{P}{T} + 3.73 \times 10^5 \frac{P_w}{T^2}, \quad (\text{A2})$$

where T is the air temperature (K), P is the total air pressure (hPa), and P_w is the water vapor pressure (hPa). We note that the constants in Eq. (A2) are empirically determined (Smith and Weintraub 1953). We use Eq. (A2) to project the model variables T , P , and P_w to refractivity and refractive index. To analyze Eq. (A1),

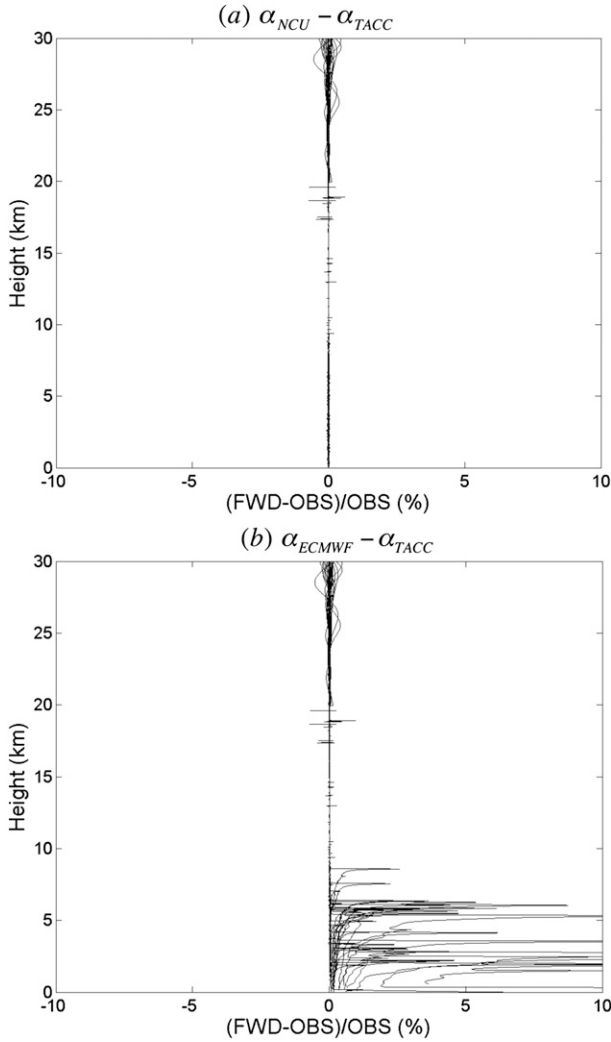


FIG. A1. (a) Relative difference of the simulated bending computed with the NCU local operator and the TACC atmPrf data. (b) As in (a), but the simulated bending angle is computed with the ECMWF-ROPP local operator.

we do not use the approximations of $[\ln n \approx 10^{-6}N]$ and $[\sqrt{x^2 - a^2} \approx \sqrt{2a(x - a)}]$ as those shown in Healy and Thépaut [2006, their Eqs. (3)–(5)]; instead, we factor the equation directly. The denominator term $\sqrt{(x^2 - a^2)}$ can be split into two terms $[\sqrt{(x + a)(x - a)}]$. Then we assume that the x in $\sqrt{(x + a)}$ is an average in levels of i th and $(i + 1)$ th. By approximating the gradient of $\ln n$ with respect to x (i.e., $d \ln n / dx$) and $x + a$ ($= \bar{x} + a = [(x_i + x_{i+1})/2] + a$) as constants for a profile, the section of the ray path between the i th and $(i + 1)$ th model levels can be written as

$$\Delta\alpha = -2a \frac{d \ln n}{dx} \frac{1}{\sqrt{\bar{x} + a}} \int_{x_i}^{x_{i+1}} \frac{1}{\sqrt{(x - a)}} dx. \quad (\text{A3})$$

Equation (A3) is used to integrate from a to the model top. Above the model top, the bending angle is computed by extrapolating the uppermost model parameters as presented in Healy and Thépaut (2006):

$$\begin{aligned} \Delta\alpha_{\text{top}} = & 10^{-6} \sqrt{2\pi a k_i N_{\text{top}}} \\ & \times \exp[k_i(x_{\text{top}} - a)] \left[1 - \text{erf}\left(\sqrt{k_i(x_{\text{top}} - a)}\right) \right], \end{aligned} \quad (\text{A4})$$

where $k_i = [\ln(N_i/N_{i+1})/(x_{i+1} - x_i)]$ and is assumed constant for a profile. And, erf represents the Gaussian error function. In Eq. (A4), k_i is set to be a constant $1/6000$ to simplify the calculation. In global models with a high domain top (e.g., 60 km or higher), the error in contribution by Eq. (A3) is very small. The error may increase for regional models with a lower top of 30 km, and this is taken care of by using Eq. (A4) to account for the high atmosphere above 30 km in this study. The uncertainty associated with the use of a lower top in the regional model is further discussed in section 5c. In the following, we refer to this new local bending angle operator as the NCU local operator.

The NCU bending angle operator is compared with that derived from the ECMWF Radio Occultation Processing Package (ROPP) operator used by Healy and Thépaut (2006), and both results are also compared with observations. The simulated bending angle with the NCU local operator is denoted as “NCU bending angle” (α_{NCU}) and the same for the “ECMWF” bending angle (α_{ECMWF}). The verification data are collected from 29 RO profiles of refractivity data from the Taiwan Analysis Center for COSMIC (TACC) on 15 June 2008. The data are in the NetCDF (atmprf) format with a vertical resolution of around 3–5 m (details of the data format can be found online at <http://tacc.cwb.gov.tw/en/>). The TACC refractivity with a coverage top of 60 km is provided as the inputs for the two local bending angle operators and the simulated bending angles are then compared with the retrieved (i.e., observed) bending angles from TACC.

Our results suggest that the simulated bending angles from both local operators are quite reliable compared to the observed values and that the simulated errors can be as low as 0.1% below 30 km. Figure A1 shows the relative differences between the simulated bending angle and observations. With this high vertical resolution, the simulated bending angle by the NCU local operator is very accurate ($<0.2\%$, about 10^{-5} rad) but the ECMWF operator provides a much larger positive bias ($\sim 10\%$) below 10 km (Figs. A1a,b). We note that the vertical

resolution of the refractivity can significantly modify the accuracy of the computed bending angle. The differences with the observations become much larger (10^{-3} rad) when the RO profile with a lower vertical resolution is used for comparison. S. B. Healy (2011, personal communication) points out that the large positive bias shown in Fig. A1b may be related to the assumption of exponential variation of refractivity in vertical. If the profiles that violate such an assumption are not used for verification, the positive bias resulting from using the ECMWF bending angle operator can be largely reduced (but cannot be completely removed). With these selected profiles, the accuracy of the NCU bending angle is only $\sim 1\%$ – 2% better. We have to emphasize that the comparisons made above use the “TACC refractivity” as the inputs. When using the bending angle operator in the assimilation system, the refractivity needs to be computed based on the model variables with Eq. (A2). Also, the vertical resolution of the model and the assumption for a local operator would introduce errors in the simulated refractivity.

REFERENCES

- Anderson, J. L., and S. L. Anderson, 1999: A Monte Carlo implementation of the nonlinear filtering problem to produce ensemble assimilations and forecasts. *Mon. Wea. Rev.*, **127**, 2741–2758, doi:10.1175/1520-0493(1999)127<2741:AMCIOT>2.0.CO;2.
- Anlauf, H., D. Pingel, and A. Rhodin, 2011: Assimilation of GPS Radio Occultation data at DWD. *Atmos. Meas. Tech.*, **4**, 1105–1113, doi:10.5194/amt-4-1105-2011.
- Anthes, R. A., and Coauthors, 2008: The COSMIC/FORMOSAT-3 mission: Early results. *Bull. Amer. Meteor. Soc.*, **89**, 313–333, doi:10.1175/BAMS-89-3-313.
- Aparicio, J. M., G. Godelieve, L. Garand, and S. Laroche, 2009: Signature of the atmospheric compressibility factor in COSMIC, CHAMP, and GRACE radio occultation data. *J. Geophys. Res.*, **114**, D16114, doi:10.1029/2008JD011156.
- Baker, N., 2011: Overview of Navy atmospheric data assimilation activities. *Ninth JCSDA Workshop on Satellite Data Assimilation*, College Park, MD, JCSDA. [Available online at http://www.jcsda.noaa.gov/meetings_Wkshp2011_Agenda.php.]
- Barker, D. M., W. Huang, Y.-R. Guo, A. J. Bourgeois, and Q. N. Xiao, 2004: A three-dimensional variational data assimilation system for use with MM5: Implementation and initial results. *Mon. Wea. Rev.*, **132**, 897–914, doi:10.1175/1520-0493(2004)132<0897:ATVDAS>2.0.CO;2.
- Chen, C.-S., and Y.-L. Chen, 2003: The rainfall characteristics of Taiwan. *Mon. Wea. Rev.*, **131**, 1323–1341, doi:10.1175/1520-0493(2003)131<1323:TRCOT>2.0.CO;2.
- , —, C.-L. Liu, P.-L. Lin, and W.-C. Chen, 2007: Statistics of heavy rainfall occurrences in Taiwan. *Wea. Forecasting*, **22**, 981–1002, doi:10.1175/WAF1033.1.
- Chen, S.-Y., C.-Y. Huang, Y.-H. Kuo, Y.-R. Guo, and S. Sokolovskiy, 2009: Assimilation of GPS refractivity from FORMOSAT-3/COSMIC using a nonlocal operator with WRF 3DVAR and its impact on the prediction of a typhoon event. *Terr. Atmos. Oceanic Sci.*, **20**, 133–154, doi:10.3319/TAO.2007.11.29.01(F3C).
- , —, —, and S. Sokolovskiy, 2010: Observational error estimation of FORMOSAT-3/COSMIC GPS radio occultation data. *Int. Workshop on Occultations for Probing Atmosphere and Climate*, Graz, Austria, ESA. [Available online at http://www.uni-graz.at/opac2010/pdf_abstracts/opac_2010_chen_shu-ya_abstract12.pdf.]
- , —, —, and —, 2011: Observational error estimation of FORMOSAT-3/COSMIC GPS radio occultation data. *Mon. Wea. Rev.*, **139**, 853–865, doi:10.1175/2010MWR3260.1.
- Ciesielski, P. E., and Coauthors, 2010: Quality-controlled upper-air sounding dataset for TiMREX/SoWMEX: Development and corrections. *J. Atmos. Oceanic Technol.*, **27**, 1802–1821, doi:10.1175/2010JTECHA1481.1.
- Cucurull, L., and J. C. Derber, 2008: Operational implementation of COSMIC observations into NCEP’s global data assimilation system. *Wea. Forecasting*, **23**, 702–711, doi:10.1175/2008WAF2007070.1.
- , Y.-H. Kuo, D. Barker, and S. R. H. Rizvi, 2006: Assessing the impact of simulated COSMIC GPS radio occultation data on weather analysis over the Antarctic: A case study. *Mon. Wea. Rev.*, **134**, 3283–3296, doi:10.1175/MWR3241.1.
- , J. C. Derber, R. Treadon, and R. J. Purser, 2007: Assimilation of global positioning system radio occultation observations into NCEP’s global data assimilation system. *Mon. Wea. Rev.*, **135**, 3174–3193, doi:10.1175/MWR3461.1.
- , —, and R. J. Purser, 2013: A bending angle forward operator for global positioning system radio occultation measurements. *J. Geophys. Res. Atmos.*, **118**, 14–28, doi:10.1029/2012JD017782.
- Davis, C. A., and W.-C. Lee, 2012: Mesoscale analysis of heavy rainfall episodes from SoWMEX/TiMREX. *J. Atmos. Sci.*, **69**, 512–537, doi:10.1175/JAS-D-11-0120.1.
- Dudhia, J., 1989: Numerical study of convection observed during the winter monsoon experiment using a mesoscale two-dimensional model. *J. Atmos. Sci.*, **46**, 3077–3107, doi:10.1175/1520-0469(1989)046<3077:NSOCOD>2.0.CO;2.
- Grell, G. A. and D. Dévényi, 2002: A generalized approach to parameterizing convection combining ensemble and data assimilation techniques. *Geophys. Res. Lett.*, **29**, doi:10.1029/2002GL015311.
- Healy, S. B., 2008: Forecast impact experiment with a constellation of GPS radio occultation receivers. *Atmos. Sci. Lett.*, **9**, 111–118, doi:10.1002/asl.169.
- , and J.-N. Thépaut, 2006: Assimilation experiments with CHAMP GPS radio occultation measurements. *Quart. J. Roy. Meteor. Soc.*, **132**, 605–623, doi:10.1256/qj.04.182.
- , J. R. Eyre, M. Hamrud, and J.-N. Thépaut, 2007: Assimilating GPS radio occultation measurements with two-dimensional bending angle observation operators. *Quart. J. Roy. Meteor. Soc.*, **133**, 1213–1227, doi:10.1002/qj.63.
- Hong, S.-Y., Y. Noh, and J. Dudhia, 2006: A new vertical diffusion package with an explicit treatment of entrainment processes. *Mon. Wea. Rev.*, **134**, 2318–2341, doi:10.1175/MWR3199.1.
- Huang, C.-Y., Y.-H. Kuo, S.-H. Chen, and F. Vandenbergh, 2005: Improvements on typhoon forecast with assimilated GPS occultation refractivity. *Wea. Forecasting*, **20**, 931–953, doi:10.1175/WAF874.1.
- , and Coauthors, 2010: Impact of GPS radio occultation data assimilation on regional weather predictions. *GPS Solutions*, **14**, 35–49, doi:10.1007/s10291-009-0144-1.
- Hunt, B. R., E. J. Kostelich, and I. Szunyogh, 2007: Efficient data assimilation for spatiotemporal chaos: A Local Ensemble

- Transform Kalman Filter. *Physica D*, **230**, 112–126, doi:10.1016/j.physd.2006.11.008.
- Jou, B. J.-D., W.-C. Lee, and R. H. Johnson, 2011: An overview of SoWMEX/TiMREX and its operation. *The Global Monsoon System: Research and Forecast*, 2nd ed. C.-P. Chang et al., Eds., World Scientific, 303–318.
- Kalnay, E., 2003: *Atmospheric Modeling, Data Assimilation and Predictability*. Cambridge University Press, 341 pp.
- Kueh, M.-T., C.-Y. Huang, S.-Y. Chen, S.-H. Chen, and C.-J. Wang, 2009: Impact of GPS radio occultation refractivity soundings on a simulation of Typhoon Bilis (2006) upon landfalling. *Terr. Atmos. Oceanic Sci.*, **20**, 115–131, doi:10.3319/TAO.2008.01.21.03(F3C).
- Kuo, Y.-H., S. Sokolovskiy, R. A. Anthes, and F. Vandenberghe, 2000: Assimilation of GPS radio occultation data for numerical weather prediction. *Terr. Atmos. Oceanic Sci.*, **11**, 157–186.
- Kursinski, E., G. Hajj, J. Schofield, R. Linfield, and K. Hardy, 1997: Observing earth's atmosphere with radio occultation measurements using the Global Positioning System. *J. Geophys. Res.*, **102**, 23 429–23 465, doi:10.1029/97JD01569.
- Lai, H.-W., C. A. Davis, and B. J.-D. Jou, 2011: A subtropical oceanic mesoscale convective vortex observed during SoWMEX/TiMREX. *Mon. Wea. Rev.*, **139**, 2367–2385, doi:10.1175/2010MWR3411.1.
- Liu, H., J. Anderson, and Y.-H. Kuo, 2012: Improved analyses and forecasts of Hurricane Ernesto's genesis using radio occultation data in an ensemble filter assimilation system. *Mon. Wea. Rev.*, **140**, 151–166, doi:10.1175/MWR-D-11-00024.1.
- Ma, Z., Y.-H. Kuo, B. Wang, W.-S. Wu, and S. Sokolovskiy, 2009: Comparison of local and nonlocal observation operators for the assimilation of GPS RO data with the NCEP GSI system: An OSSE study. *Mon. Wea. Rev.*, **137**, 3575–3587, doi:10.1175/2009MWR2809.1.
- , —, and —, 2011: Assimilation of GPS radio occultation data for an intense atmospheric river with the NCEP regional GSI system. *Mon. Wea. Rev.*, **139**, 2170–2183, doi:10.1175/2011MWR3342.1.
- Mlawer, E. J., S. J. Taubman, P. D. Brown, M. J. Iacono, and S. A. Clough, 1997: Radiative transfer for inhomogeneous atmosphere: RRTM, a validated correlated-k model for the longwave. *J. Geophys. Res.*, **102**, 16 663–16 682, doi:10.1029/97JD00237.
- Skamarock, W. C., and J. B. Klemp, 2008: A time-split non-hydrostatic atmospheric model for weather research and forecasting applications. *J. Comput. Phys.*, **227**, 3465–3485, doi:10.1016/j.jcp.2007.01.037.
- Smith, E. K., and S. Weintraub, 1953: The constants in the equation for the atmospheric refractive index at radio frequencies. *Proc. IRE*, **41**, 1035–1037, doi:10.1109/JRPROC.1953.274297.
- Sokolovskiy, S., 2003: Effect of superrefraction on inversions of radio occultation signals in the lower troposphere. *Radio Sci.*, **38**, 1058, doi:10.1029/2002RS002728.
- , Y.-H. Kuo, and W. Wang, 2005a: Assessing the accuracy of a linearized observation operator for assimilation of radio occultation data: Case simulations with a high-resolution weather model. *Mon. Wea. Rev.*, **133**, 2200–2212, doi:10.1175/MWR2948.1.
- , —, and —, 2005b: Evaluation of a linear phase observation operator with CHAMP radio occultation data and high-resolution regional analysis. *Mon. Wea. Rev.*, **133**, 3053–3059, doi:10.1175/MWR3006.1.
- Tao, W.-K., and Coauthors, 2003: Microphysics, radiation and surface processes in the Goddard Cumulus Ensemble (GCE) model. *Meteor. Atmos. Phys.*, **82**, 97–137, doi:10.1007/s00703-001-0594-7.
- Torn, R. D., G. J. Hakim, and C. Snyder, 2006: Boundary conditions for limited-area ensemble Kalman filters. *Mon. Wea. Rev.*, **134**, 2490–2502, doi:10.1175/MWR3187.1.
- Tu, C.-C., Y.-L. Chen, C.-S. Chen, P.-L. Lin, and P.-H. Lin, 2014: A comparison of two heavy rainfall events during the Terrain-Influenced Monsoon Rainfall Experiment (TiMREX) 2008. *Mon. Wea. Rev.*, **142**, 2436–2463, doi:10.1175/MWR-D-13-00293.1.
- Vergados P., A. J. Mannucci, and H. Su, 2013: A validation study for GPS radio occultation data with moist thermodynamic structure of tropical cyclones. *J. Geophys. Res. Atmos.*, **118**, 9401–9413, doi:10.1002/jgrd.50698.
- Xu, W., E. J. Zipser, Y.-L. Chen, C. Liu, Y.-C. Liou, W.-C. Lee, and B. J.-D. Jou, 2012: An orography-associated extreme rainfall event during TiMREX: Initiation, storm evolution, and maintenance. *Mon. Wea. Rev.*, **140**, 2555–2574, doi:10.1175/MWR-D-11-00208.1.
- Yang, S.-C., E. Kalnay, and T. Miyoshi, 2012: Improving EnKF spin-up for typhoon assimilation and prediction. *Wea. Forecasting*, **27**, 878–897, doi:10.1175/WAF-D-11-00153.1.
- , K.-J. Lin, T. Miyoshi, and E. Kalnay, 2013: Improving the spin-up of regional EnKF for typhoon assimilation and forecasting with Typhoon Sinlaku (2008). *Tellus*, **65A**, 20804, doi:10.3402/tellusa.v65i0.20804.